Dynamic profiling and functional interpretation of histone Kcr and Kla during neural development

Shang-Kun Dai[1,2,4], Pei-Pei Liu[1,2,3,5], Xiao Li[1,2,3,5], Lin-Fei Jiao[1,2,3,5], Zhao-Qian Teng[1,2,3,5] and Chang-Mei Liu[1,2,3,5,]*

[1] State Key Laboratory of Stem Cell and Reproductive Biology, Institute of Zoology, Chinese Academy of Sciences, Beijing 100101, China

[2] Savaid Medical School, University of Chinese Academy of Sciences, Beijing 100049, China

[3] Institute for Stem Cell and Regeneration, Chinese Academy of Sciences, Beijing 100101, China

[4] School of Life Sciences and Medicine, Shandong University of Technology, Zibo 255049, China

[5] Beijing Institute for Stem Cell and Regenerative Medicine, Beijing 100101, China

*Author for correspondence Tel: +86 10 82619690; Email: liuchm@ioz.ac.cn

Key words: Histone crotonylation, histone lactylation, neural development, neuronal fate, histone deacetylases

Summary statement: Non-acetyl novel histone lysine acylations such as histone Kcr and Kla are tightly correlated with neuronal fate during neural development via transcriptome remodeling.

ABSTRACT

Metabolites such as crotonyl-CoA and lactyl-CoA influence gene expression by covalently modifying histones, known as histone lysine crotonylation (Kcr) and lysine lactylation (Kla). However, their existence patterns, dynamic changes, biological functions，and associations with histone lysine acetylation and gene expression during mammalian development remain largely unknown. Here, we find that histone Kcr and Kla are widely distributed in the brain and undergo global changes during neural development. By profiling genome-wide dynamics of H3K9ac, H3K9cr and H3K18la in combination with ATAC and RNA sequencing, we reveal that these marks are tightly correlated with chromatin state and gene expression, and extensively involved in transcriptome remodeling to promote cell-fate transitions in the developing telencephalon. Importantly, we demonstrate that global Kcr and Kla levels are not the consequence of transcription and identify histone deacetylase (HDAC)1-3 as novel "erasers" of H3K18la. Using P19 cells as induced neural differentiation system, we find that HDAC1-3 inhibition by MS-275 pre-activates neuronal transcriptional programs through stimulating multiple histone lysine acylations simultaneously. These findings suggest histone Kcr and Kla play critical roles in the epigenetic regulation of neural development.

INTRODUCTION

The N-terminal tails of histones are subjected to various post-translational modifications (PTMs), which shape the local chromatin landscape to regulate transcription, replication, DNA repair, and higher-order chromatin structure (Diehl and Muir, 2020; Klemm et al., 2019). Some metabolites including propionyl-CoA, butyl-CoA, crotonyl-CoA, lactyl-CoA, 2-hydroxyisobutyl-CoA, β-hydroxybutyryl-CoA, succinyl-CoA, benzoyl-CoA, malonyl-CoA, and glutaryl-CoA have recently been identified as donors for histone PTMs to influence gene expression (Diehl and Muir, 2020; Li et al., 2018). Among these, crotonyl-CoA

and lactyl-CoA, which act as substrates for histone lysine crotonylation (Kcr) and lysine lactylation (Kla) catalyzed by CBP/p300, respectively (Sabari et al., 2015; Zhang et al., 2019). Histone Kcr and Kla have attracted great attention due to their emerging roles in linking cellular metabolism and epigenetic regulation to orchestrate gene expression, cell state transition, and disease process (Li and Wang, 2021; Li et al., 2020; Yu et al., 2021; Zhang et al., 2019).

Kcr and Kla can occur on all core histone proteins, and they share the most common modification sites with Kac (Tan et al., 2011; Zhang et al., 2019). Over the last five years, regulatory mechanisms for histone Kcr have been thoroughly elucidated, including its "writers" (enzymes in charge of catalyzing Kcr) (Kollenstart et al., 2019; Liu et al., 2017c; Sabari et al., 2015), "erasers" (enzymes responsible for removing Kcr) (Fellows et al., 2018; Kelly et al., 2018; Wei et al., 2017), "readers" (enzymes capable of recognizing Kcr) (Andrews et al., 2016; Li et al., 2016; Xiong et al., 2016; Zhao et al., 2016), and metabolic regulators (enzymes involving in crotonyl-CoA metabolism) (Fang et al., 2021; Jiang et al., 2018; Liu et al., 2017b; Liu et al., 2019; Sabari et al., 2015; Tang et al., 2021), which extend our knowledge about versatile functions of histone Kcr. Recent studies have revealed that p300 and glycolysis are major pathways to regulate histone Kla levels, and that H3K18la involves in M1 macrophage polarization, cell reprograming, and tumorigenesis (Li et al., 2020; Yu et al., 2021; Zhang et al., 2019). Both histone Kcr and Kla can directly stimulate transcription in a cell free system (Sabari et al., 2015; Zhang et al., 2019). Specifically, recognition of H3K9cr, H3K18cr, and H3K27cr by YEATS domain of AF9 may regulate transcription process through recruiting the Super Elongation Complex (SEC) and Dot1L complex (DOT1LC) (Li et al., 2016; Li et al., 2014; Luo et al., 2012). However, it is unclear whether histone Kcr and Kla are causal or consequential for transcription under physiological conditions.

Genome-wide associations between histone Kcr and gene expression have been investigated in various organisms, which consistently suggest that histone Kcr is a widely distributed mark of active chromatin (Crespo et al., 2020; Fellows et al., 2018; Gowans et al., 2019; Kelly et al., 2018; Lu et al., 2018; Sabari et al., 2015; Tan et al.,

2011). In addition, histone Kla is associated with inflammation and oncogenesis-related transcriptional programs (Yu et al., 2021; Zhang et al., 2019). However, it remains unknown whether and how histone Kcr and Kla are involved in transcription regulation during mammalian development. Considering important roles of histone Kac in neurodevelopment and neurological diseases (Li et al., 2019; Tang et al., 2019; Wang et al., 2010; Yao et al., 2016), the associations of histone Kcr and Kla with gene expression and their biological functions merit further investigation. Moreover, there is growing evidence that HDACs regulate multiple histone deacylation reactions except deacetylation (Huang et al., 2018; Huang et al., 2021; Wei et al., 2017), but little is known about how different histone acylations are coordinated to regulate gene expression and biological process when HDACs are perturbed.

In this study, we systematically investigate the dynamic changes of histone Kcr and Kla and their associations with gene expression, as well as the interplays among histone acylations during neural development. We observe the global existence and significant changes of histone Kcr and Kla in the developing telencephalon. Further multi-omics profiling uncovers that H3K9cr and H3K18la mark transcriptionally active chromatin both in vivo and in vitro. There are distinct patterns for genome-wide alterations in H3K9ac, H3K9cr, and H3K18la, but integrated analysis of chromatin immunoprecipitation-sequencing (ChIP-seq) and RNA-seq data across different developmental stages reveals that these histone marks are extensively involved in transcriptome remodeling to favor neural differentiation. In addition, inhibition of transcription does not influence global histone Kcr and Kla levels. Finally, we discover that inhibition of HDAC1-3 promotes neuronal transcriptional programs by multiple histone acylations.

RESULTS

Changes in global histone Kcr and Kla during neural development

We firstly determined the presence of Kcr and Kla in the H3 N-terminal tails during neural development, and found that histone Kcr and Kla displayed extensive existence in the embryonic cortex (Fig. 1A). Kcr and Kla could be observed in TUJ1^{+} neurons in the intermediate zone and cortical plate regions, and TUJ1^{-} neural progenitor cells in the ventricular/subventricular zone (Fig. 1A). By quantifying the enrichment level of these modifications across the layers of cortex, we found that H3K9cr and H3K18la levels were significantly higher in the cortical plate regions than that in the ventricular/subventricular zone (Fig. 1B; Fig. S1A). Next, we examined the levels of these histone marks across different developmental stages (Fig. 1C), and found that H3K9cr levels increased but H3K18la and H3-Kla levels reduced at the late-stage of neurogenesis compared with that at the early-stage of neurogenesis, however, there were no apparent changes in H3K18cr, H3K14la, and H3-Kcr levels (Fig. 1D-F).

We then checked changes in these histone marks at the cellular level (Fig. S1B) and observed that the levels of H3K18cr and H3K18la, but not that of H3K9cr and H3K14la declined sharply during neural differentiation of P19 EC cells (Fig. S1C, D), indicating different dynamics of site-specific histone acylations during cell fate transitions. Altogether, these results suggest that histone Kcr and Kla are widely distributed and undergo global changes during neural development.

Multi-omics profiling and functional interpretation of H3K9cr and H3K18la

In order to explore the chromatin function of histone Kcr and Kla during neural development, we performed specific anti-H3K9ac, anti-H3K9cr, and anti-H3K18la (lactylation is not found at H3K9 site in mouse cells) ChIP-seq assays by using highly specific antibodies (Fig. S2) to analyze telencephalon at E13.5 (Zhang et al., 2019), and obtained highly reproducible sequencing data (Fig. S3A). First, H3K9ac and H3K9cr were mainly located in promoter regions, while H3K18la was mostly

enriched in intron and intergenic regions (Fig. 2A). Next, k-means clustering divided annotated genes into distinct chromatin environments by the H3K9ac signal (Fig. 2B). Genes with high levels of H3K9ac were usually accompanied by high levels of H3K9cr, H3K18la, chromatin accessibility, and gene expression (Fig. 2B). In addition, H3K9ac-marked genes were also mostly regulated by H3K9cr and H3K18la (Fig. S3B), and genes with all three marks displayed higher chromatin accessibility in their promoter regions and higher gene expression levels than that of the mono-marked genes (Fig. 2C). These results suggested that multiple histone acylations might co-regulate transcriptionally active chromatin.

In our analysis, we found that there were many genes annotated in histone acylations peaks to precisely uncover its predominately involved biological processes (Fig. S4A). Therefore, we divided H3K9ac, H3K9cr, and H3K18la peaks into three clusters based on their modification levels to explore the biological functions of these histone marks (Fig. S4A). Interestingly, genes in cluster 1 with the strongest H3K9ac and H3K9cr intensity were involved in RNA and protein metabolism and neurodegenerative disorders-related pathways (Fig. S4B; Fig. 2D). By contrast, genes with the highest H3K18la levels were mainly involved in cell proliferation-related pathways (Fig. 2D). De novo motif analysis for peak regions of these modifications revealed several transcription factors, such as ELK4 and SOX10, which are important regulators of neural development (Fig. S4C-E). Consistent with in vivo data, we found the wide distributions (Fig. S5A), tight interplays (Fig. S5B, C), and participated functions (Fig. S5D) of these modifications in P19 EC cells-derived NSPCs by ChIP-seq assays. Collectively, these results indicate that H3K9ac, H3K9cr, and H3K18la are tightly correlated with chromatin state and gene expression, but they are involved in different signaling pathways both in vivo and in vitro.

Genome-wide changes in H3K9cr and H3K18la favor neural differentiation

Histone PTMs undergo dynamic changes and play important roles in embryonic neurogenesis during which NSPCs exit cell cycle and differentiate into neurons (Yao et al., 2016). However, it is still not clear how histone Kcr and Kla participate in this process. Thus, we systemically analyzed genome-wide changes in H3K9ac, H3K9cr, and H3K18la at early (E13.5) and late (E16.5) stages of embryonic neurogenesis by ChIP-seq (Fig. S3A) and RNA-seq (Fig. S6). We found positive correlations between changes in H3K9ac, H3K9cr, and H3K18la and altered gene expression (Fig. S7A-C). Compared with H3K9ac and H3K9cr, we discovered that H3K18la enrichment declined significantly in promoter regions of genes encoding histones which play important roles during cell proliferation (Fig. S7D) (Marzluff and Koreski, 2017). Importantly, genes with enrichments of all three marks displayed higher expression changes than those with alterations of mono-mark (Fig. S7E, F).

We next assessed the peaks with differential histone acylations during neural development. There were different patterns for changes in differential peaks and regulated genes among these histone marks (Fig.3A, B; Fig.S8A, B). Specifically, compared with H3K9cr and H3K18la, the numbers of peaks and genes with increased H3K9ac enrichment were the most (Fig.3A; Fig. S8A), while the numbers of peaks and genes with reduced H3K9ac enrichment were the lowest (Fig.3B; Fig. S8B). However, predicted biological processes of genes with differential histone marks were highly consistent with neural development (Fig.S8C, D). To correlate the alterations in histone acylations with gene expression changes, we performed binding and expression target analysis (BETA) (Wang et al., 2013) and found that peaks with increased H3K9cr and H3K18la had significant effects as a gene activator (Fig. 3C-F), while peaks with reduced H3K9cr and H3K18la had significant effects as a gene repressor (Fig.S9). Further enrichment analysis indicated that upregulated genes with increased H3K9cr or H3K18la enrichment were mainly involved in neuronal differentiation and maturation (Fig. 3G, H; Fig.S10), while downregulated genes with reduced H3K9cr or H3K18la enrichment were tightly associated with cell proliferation (Fig.S9E, F). Collectively, these data support that H3K9ac, H3K9cr, and

H3K18la might undergo genome-wide alterations and extensively involve in gene expression changes associated with neural differentiation in vivo.

Transcriptional repression has no effect on global histone Kcr and Kla levels

A recent study shows that inhibition of transcription results in the loss of histone Kac in bulk histones, and the majority of histone Kac is dependent on transcription (Martin et al., 2021). However, the associations between non-acetylation histone acylations and transcription under physiological conditions are still unclear. To investigate whether global histone Kcr and Kla levels were influenced by transcription, we treated P19 EC cells-derived NSPCs with the well-studied transcription inhibitors Triptolide (inhibiting transcription initiation) and Flavopiridol (inhibiting transcription elongation) at high concentrations (Bensaude, 2011). Transcription was significantly inhibited as indicated by the loss of RNA polymerase II (RNAP2) serine 5 CTD phosphorylation (S5p) and RNAP2 serine 2 CTD phosphorylation (S2p) (Fig. 4A), and reduced nascent transcripts from the *Actb* and *Gapdh* genes (Fig. 4B). Surprisingly, we didn't detect any significant changes in H3K9cr, H3K18cr, H3K14la, and H3K18la in P19 EC cells-derived NSPCs and neurons (Fig. 4C, D), indicating that the majority of histone Kcr and Kla was not a consequence of transcription.

Inhibition of HDAC1-3 significantly increases H3K18la both in vitro and in vivo

Given the fact that some HDACs have been demonstrated to "erase" several histone acylations except Kac (Huang et al., 2018; Wei et al., 2017), we next asked whether HDACs could regulate histone Kla. To this end, we applied two pan-HDACs inhibitors (SAHA and VPA) and found that SAHA treatment increased H3K18la levels, while VPA stimulated both H3K14la and H3K18la levels in P19 EC cells (Fig.5A, B). Furthermore, we found that a selective inhibitor of HDAC1-3, MS-275, robustly promoted H3K14la and H3K18la levels compared with EX 527 (a selective SIRT1 inhibitor) (Fig. 5C). Meanwhile, we observed an increase of H3K9cr and

H3K18cr levels after SAHA, VPA, or MS-275 treatment, which was consistent with previous studies (Fig. 5A-C) (Fellows et al., 2018; Kelly et al., 2018; Wei et al., 2017).

To confirm our above findings in vivo, we injected pregnant mice with MS-275 and detected a significant increase in H3K14la and H3K18la levels, as well as an elevation in H3K9cr and H3K18cr levels (Fig. 5D-F). We next investigated whether the dynamic changes in histone Kla levels existed after interference of expression of HDACs, the results showed that simultaneous knockdown of *Hdac1-3* significantly increased H3K14la and H3K18la levels in P19 EC cells (Fig. 5G, H). Given the growing literature on regulations for histone Kcr, we explored whether knockdown of the writer (GCN5) and eraser (HDAC1-3) for H3K9cr affect histone methylation and transcription. The results showed that H3K9ac, H3K9cr, and transcription elongation (S2p) levels significantly reduced after knockdown of GCN5, while H3K9ac, H3K9cr, and transcription elongation (S2p) levels obviously increased after knockdown of HDAC1-3 (Fig. S11). However, there were no evident changes in histone methylations, such as H3K4me3, H3K9me3, and H3K27me3, and in transcription initiation (S5p) levels (Fig. S11). Overall, these results suggest that HDAC1-3 are novel histone lysine delactylases both in cells and in vivo.

Inhibition of HDAC1-3 pre-activates neuronal transcriptional programs through multiple histone acylations

H3K18la has recently been reported to regulate M1 macrophage polarization, cell reprograming, and tumorigenesis (Li et al., 2020; Yu et al., 2021; Zhang et al., 2019), however, we still don't know how H3K18la is regulated and co-operates with other histone acylations during neural stem cell fate decisions. To this end, we treated differentiating P19 EC cells with MS-275 and performed anti-H3K9ac, anti-H3K9cr, and anti-H3K18la ChIP-seq assays. Inhibition of HDAC1-3 by MS-275 induced genome-wide enhancement of H3K9ac, H3K9cr, and H3K18la (Fig.S12A-C). The increased enrichment of these histone marks suggested they acted as a gene activator

but not a gene repressor (Fig.S12D-F), and genes under regulation of these modifications were involved in neuronal differentiation and maturation (Fig. S12G-I). Genes with increased all three marks, such as *Neurod2*, were tightly associated with neural cell fate decisions (Fig.6A, B; Fig.S13A) and displayed more prominent expression alterations by comparing genes with mono-mark changes (Fig. 6C).

While taking into account gene expression changes, there were 635 upregulated genes with all three histone marks increased after MS-275 treatment (Fig. S13B), which could be divided into three clusters based on their patterns of expression changes across different timepoints of differentiation (Fig. 6D). Genes in cluster 1 were gradually up-regulated during differentiation, and were tightly associated with neuronal differentiation and pre-activated by simultaneously increased multiple histone acylations (Fig. 6D; Fig.S13C-E). In contrast, genes in cluster 2 might be associated with the development of other germ layers, because their expression levels and histone acylations enrichment were unchanged during whole differentiation processes (Fig. 6D; Fig. S13F-H). Furthermore, genes in cluster 3 were highly expressed in P19 EC cells but down-regulated during differentiation, and they might be involved in maintaining identity of P19 EC cells (Fig. 6D).

In cultured NSPCs isolated form E13.5 mice forebrain, we also validated those genes with increased histone Kac and Kcr enrichment were up-regulated after MS-275 treatment and that these genes were tightly associated with neuronal differentiation and maturation (Fig. S14, Fig.S15A). Functionally, MS-275-treated NSPCs displayed increased H3K9ac, H3K9cr, and H3K18la levels (Fig. S15B) and differentiated into more TUJ1^{+} neurons than those in the control group (Fig. S15C and D). Collectively, these results suggest that MS-275 promotes transcriptional programs associated with neuronal differentiation in differentiating P19 EC cells and NSPCs by activating multiple histone acylations simultaneously.

DISCUSSION

In this study, we for the first time profiled dynamic changes and performed functional interpretation of histone Kcr and Kla in the developing telencephalon. We demonstrated that HDAC1–3 act as novel "erasers" of H3K18la and furtherly linked multiple histone acylations with neural differentiation. First, histone Kcr and Kla exist extensively and undergo significant changes during neural development. Next, H3K9ac, H3K9cr, and H3K18la are histone PTMs marking active chromatin regions and are tightly correlated with gene expression. Systematic dissection of alterations in these histone marks across different developmental stages reveals that genome-wide dynamic changes in H3K9cr and H3K18la are extensively involved in neuronal differentiation and cell proliferation processes, which highlights the remodeling of histone acylations to orchestrate gene expression changes as well as cell fate transitions (Fig. 7A). Furthermore, we find that global levels of Kcr an Kla are not influenced by transcription inhibition. Importantly, we uncover that HDAC1-3 influence H3K18la levels, and regulate neural differentiation of P19 EC cells by multiple histone acylations (Fig. 7B).

The extensive existence and so many marked-genes of histone Kcr and Kla in the developing telencephalon indicated that histone acylations are intrinsic pathways to regulate gene expression during mammalian development. In addition, the difference in patterns of changes in H3K9ac, H3K9cr, and H3K18la is to be expected, because the levels of donors for various histone acylations may alter during neural development. For instance, there is a transition from glycolytic to mitochondrial oxidative phosphorylation during neurogenesis, so it is possible that reduction in production of lactate and lactyl-CoA may influence histone Kla levels during development (Khacho et al., 2019).

NSPCs in the embryonic forebrain with deletion of HDAC1, 2, or 3 are prone to differentiate into neurons (Li et al., 2019; Tang et al., 2019). Similarly, we found pre-activation of neuronal transcriptional programs by multiple histone acylations when HDAC1–3 was inhibited during neural differentiation of P19 EC cells. These

findings indicate that HDAC1–3 are repressors of neuronal differentiation during neural development. In contrast, CBP knockdown in cultured NSPCs inhibits their neuronal differentiation (Wang et al., 2010). H3K9/14ac are enriched at the promoter of *Tuj1* and are bound by CBP at E13, and their enrichment peaks at E16 and then decreases postnatally in the developing cortex (Wang et al., 2010). In the adult brain, CBP/p300 maintain the excitatory neuron identity through the regulation of histone Kac in cell type-specific promoter and enhancer regions (Lipinski et al., 2020). These results suggest important roles of CBP/p300 during establishment and maintenance of neuron identity. At the early stage of neurogenesis, neural differentiation-related genes are kept in primed state, and both histone acetyltransferases (HATs) and HDACs are targeted to these development-related primed genes simultaneously (Liu et al., 2017a; Wang et al., 2009). Considering the dynamic changes in histone Kac, Kcr, and Kla during neural development and the capacity of CBP/p300 to catalyze multiple histone acylations (Liu et al., 2017c; Sabari et al., 2015; Zhang et al., 2019), we propose the existence of a switch for histone acylations at regulatory elements of genes regulating neural fate decisions, which is triggered by the balance between CBP/p300 and HDACs (Fig. 7A).

Almost all studies of the causal relationship between histone Kcr/Kla and gene transcription make conclusions mainly based on the consistency between changes in histone acylations and gene expression. However, there is no evidence to support direct regulation of transcription by histone Kcr and Kla at the cellular level. In addition, whether the link between histone Kcr and Kla and transcription under physiological condition is a causal or consequential event has not been addressed previously. Although the present study can't rule out the possibility of changes of these histone marks in the local sites of the genome, our data clearly demonstrate that transcription inhibition has no effect on global histone Kcr and Kla levels, indicating that the majority of histone Kcr and Kla are not dependent on transcription. Consistently, a recent study reports that there is no global effect on histone Kac within a short time frame of transcription inhibition (Vaid et al., 2020).

At the cellular level, some HDACs have been proved to "erase" histone Kcr (HDAC1, 2, 3, 8, and SIRT1) (Wei et al., 2017), histone lysine benzoylation (SIRT2) (Huang et al., 2018), and histone lysine β-hydroxybutyrylation (HDAC1 and 2) (Huang et al., 2021). Interestingly, we find that inhibition of HDAC1−3 significantly stimulates H3K14la and H3K18la levels both in vitro and in vivo, which suggest that HDAC1−3 is novel "erasers" of histone Kla. A recent preprint study by Olsen and colleagues reports the histone delactylation activity of HDAC1-3 along with an unaltered H3K18la levels after knockdown of *HADC1−3* in HeLa cells under physiological conditions (Moreno-Yruela et al., 2021). In the present study, however, we observed a remarkably increase in H3K14la and H3K18la levels after simultaneous knockdown of *Hdac1-3* in P19 EC cells. We speculate that this discrepancy may be due to the knockdown efficiency of HDAC1-3 and specific cell types.

Convincingly, our in vivo and ChIP-seq results support the conclusion that HDAC1-3 can "erase" H3K18la at the cellular level. Functionally, genes with gain of H3K18la after MS-275 treatment are directly involved in neural differentiation (Fig. S12I). Considering that the associations between histone acylations and their biological functions are less understood (Fellows et al., 2018; Kelly et al., 2018), the present study identifies a novel link between HDACs and multiple histone acylations to regulate cell fate transitions associated transcriptional program (Fig. 7B). Future studies should focus on the crosstalk between Kcr/Kla with other histone modifications or regulatory elements, such as co-occurrence of these modifications with super-enhancers. The present study has several limitations. We did not directly determine the regulatory relationships of Kcr/Kla with neuronal fate limited to specific pathways to stimulate or block these modifications. Moreover, due to technical limitations, we still need to confirm the results from P19 EC cells-derived NSPCs in other physiological models, such as embryonic NSPCs and in vivo.

Overall, our study provides novel insights into the dynamic changes, epigenetic interactions, transcription regulation, and biological functions of histone acylations during neural development. We also bridge HDACs and multiple histone acylations

with NSPCs fate decisions, and highlight their close relationships and critical roles in the epigenetic regulation of neural development and disease.

MATERIALS and METHODS

Mice

All mice were on the ICR/CD-1 background. The pregnant mice were purchased from SiPeiFu Biotechnology Co., Ltd. (Beijing, China). All mouse experiments were approved by the Animal Committee of the Institute of Zoology, Chinese Academy of Sciences, Beijing, China.

Cell culture

P19 EC cells were obtained from the American Type Culture Collection (CRL-1825) and maintained in the proliferation medium (minimum essential medium-alpha [MEMα; Gibco] containing 10% fetal bovine serum [FBS; Gibco]) in an incubator at 37°C and 5% CO_2. For induced neural differentiation, 1×10^6 cells were cultured on a 9.6 cm bacterial-grade Petri dish in the induction medium (proliferation medium containing 1 μM all-trans retinoic acid [Sigma-Aldrich]) for 4 d, with media exchanged every 2 d. To induce neuronal differentiation, the aggregated neurospheres were digested in to single cells by Accutase (STEMCELL Technologies) and plated at a density of 1.2×10^7 cells per 10 cm culture dish (Corning) pre-coated with 0.1 mg/ml poly-D-lysine (PDL; Sigma-Aldrich) in the differentiation medium (DMEM/F12 containing with 2% B27 [Gibco]) for 4 d, with media exchanged every 2 d. 293T cells were cultured in the DMEM medium (Gibco) containing 10% fetal bovine serum. NSPCs isolated from E13.5 mice forebrain were cultured and treated with MS-275 as previously described (Dai et al., 2021). The differentiation protocols for NSPCs were also followed our published methods, but 5% FBS was employed instead of forskolin and retinoic acid in the present study (Dai et al., 2021).

Inhibitor treatment

Inhibitors were all purchased from Selleck Chemicals. P19 EC cells treatments were performed in the proliferation medium at the following concentration for 12 h or 24 h: 0.5 μM SAHA (S1047, CAS: 149647-78-9), 1 mM VPA (S3944, CAS: 99-66-1), 1 μM MS-275 (S1053, CAS: 209783-80-2), and 1 μM EX 527 (S1541, CAS: 49843-98-3). For in vivo experiment, 20 mg/kg MS-275 was injected every 24 h for two consecutive days in pregnant mice at day 13.5 of pregnancy. P19 EC cells-derived NSPCs (day 1) were treated with 1 μM MS-275 for 1 d and then collected for ChIP-seq and RNA-seq assays. P19 EC cells-derived NSPCs (day 2) treatments were performed in the induced medium at the follow concentration for 1 h: 5 μM Triptolide (S3604, CAS: 38748-32-2) and 5 μM Flavopiridol HCl (S2679, CAS: 131740-09-5).

Cell transfection

P19 EC cells were transfected with double-strand siRNA using Lipofectamine RNAiMAX transfection regent (Invitrogen) with the final concentration of 50 nM for 3 days and then collected for western blot assay. 293T cells were transfected with siRNA using Lipofectamine 3000 transfection regent (Invitrogen) with the final concentration of 50 nM for 2 days and then collected for western blot assay. The negative control siRNA (siR NC #1, siN0000001-1-5) and siRNA targeting *Hdac1* (si-m-Hdac1_004, siB140729172936), *Hdac2* (si-m-Hdac2_004, siB140729171225), *Hdac3* (si-m-Hdac3_001, siG141217112523), and *GCN5/KAT2A* (si-h-KAT2A_004, siB14815190908) were purchased from Ribobio Co., Ltd. (Guangzhou, China).

Immunocytochemistry staining

DAPI (Sigma-Aldrich) was used to label cell nuclei. For immunocytochemistry analysis, cells on coverslips were fixed in 4% formaldehyde for 15 min at room temperature and then washed three times with phosphate-buffered saline (PBS). Next,

cells were incubated with blocking solution (2% bovine serum albumin and 0.3% Triton X-100) at room temperature for 1 h. Coverslips were then incubated with primary antibodies diluted in blocking solution at 4°C overnight and labeled using appropriate secondary antibodies at room temperature for 2 h. For immunostaining, embryonic mouse brains were cut into 12 μm thick cryosections using Leica CM 1950. Staining procedures for brain slices were the same as those used for immunocytochemistry analysis. Detailed information on the primary and secondary antibodies used for immunocytochemistry and immunostaining analysis is summarized in Table S1. All images were acquired using confocal microscopy (Zeiss, LSM710 and LSM880). For quantitative analysis of enrichment levels of histone acylations in Fig. 1B, three 40 μm × 40 μm bins were randomly selected across each layer of cortex, then ImageJ was used to perform quantitative analysis of mean fluorescence intensity.

Western blot and dot blot assays

Total proteins were extracted using the RIPA lysis buffer (Beyotime Biotechnology, Shanghai, China) containing 1 × protease inhibitor cocktail (Bimake). Nuclear proteins were acquired as previously described (Dai et al., 2021), and protein concentrations were measured using a BCA protein assay kit (Beyotime). Histones were isolated from cells and tissues following standard acid extraction protocols (Shechter et al., 2007), and their concentrations were determined using the Bradford protein assay kit (Beyotime). In briefly, cells and tissues were incubated with extraction buffer (PBS with 0.5% Triton X-100, 1 mM PMSF, and 5 mM sodium butyrate) with gentle rotation at 4°C for 10 min, and nuclei were isolated by centrifugation (1500 g for 10 min at 4°C). Next, 0.4 M HCL was used to resuspend nuclei, followed by incubation on ice for 30 min, soluble histones were isolated by centrifugation (20,000 g for 10 min at 4°C).

Proteins were separated using 6–15% SDS-PAGE and transferred onto polyvinylidene fluoride (PVDF) membranes (Millipore). Blotted membranes were blocked in 5% skim milk (BD Biosciences) in Tris-buffered saline with 0.1% Tween 20

(TBS-T) and incubated with primary antibodies at 4°C overnight. Membranes were then washed three times with TBS-T and incubated with secondary antibodies at room temperature for 1–2 h. The immunoreactive products were detected using SuperSignal West Pico PLUS Chemiluminescent Substrate (Thermo Scientific) and a Tanon-5200 Chemiluminescent Imaging System (Tanon, Shanghai, China). ImageJ was used to perform quantitative analysis of western blot results as the ratio of target histone marks or protein gray value to the gray value of reference proteins (H3, β-Actin or β-Tubulin). For dot blot assay, peptide samples were spotted onto PVDF membranes, which were first blocked at room temperature for 1 h and then washed in TBS-T. Primary and secondary antibodies were incubated at room temperature for 2 h and 45 min, respectively, followed by washing three times with TBS-T and signal detection. Detailed information on the primary and secondary antibodies used for western blot assay is summarized in Table S1.

qRT-PCR

RNA was extracted using Trizol reagent (Invitrogen), then RNA samples were subjected to qRT-PCR using a Roche LightCycler 480 II. In brief, total RNA was transcribed into cDNA using the TransScript One-Step gDNA Removal and cDNA Synthesis Kit (TransGen Biotech, Beijing, China) with random primer. For qRT-PCR analysis, cDNA was quantified by using Hieff qPCR SYBR Green Master Mix (YEASEN, Shanghai, China) in a 20-μl reaction system according to instructions, PCR steps were performed 5 min initial pre-denaturation at 95 °C, followed by 45 cycles of each 10 s at 95 °C, 30 s at 60 °C, 30 s at 72 °C and samples were run in triplicate. The relative expression was calculated using the $2^{-\Delta\Delta Ct}$ method. The PCR primers were designed to target both exon and intronic regions to capture nascent transcripts of *Actb* and *Gapdh*, and their sequence was provided in Table S2.

ATAC-seq and RNA-seq

We used the TruePrep DNA Library Prep Kit V2 for Illumina (Vazyme, Nanjing, China) to construct ATAC-seq libraries in two biological replicates. In brief, a total of 5×10^4 cells (P19 EC cells-derived NSPCs and digested telencephalon cells at E13.5) were lysed in 50 μL lysis buffer (10 mM Tris-HCl [pH 7.4], 10 mM NaCl, 3 mM MgCl$_2$, and 0.5% NP-40) on ice for 10 min. The suspension was then centrifuged at 500 g for 5 min at 4°C, following by addition of 50 μL trans-position reaction mix containing 5 × TTBL and TTE Mix V50 to incubate at 37°C for 30 min. After tagmentation, fragmented DNA was purified with 100 μL VAHTS DNA clean beads (Vazyme) and amplified for 12 cycles using the following PCR conditions: 72°C for 3 min; 98°C for 30 s; and thermocycling at 98°C for 15 s, 60°C for 30 s and 72°C for 30 s; following by 72°C for 5 min. After PCR amplification, libraries were purified and selected by DNA clean beads. Libraries were then sequenced on Illumina platforms by Annoroad Gene Technology Co., Ltd. (Beijing, China).

mRNA-seq was performed in two biological replicates. Briefly, RNA was extracted using Trizol reagent (Invitrogen), and mRNA was purified from total RNA using poly T oligo-attached magnetic beads. Libraries were then constructed using the NEBNext Ultra RNA Library Prep Kit for Illumina (NEB), following the manufacturer's instructions, and sequenced on Illumina platforms by Annoroad Gene Technology Co., Ltd.

Native ChIP-seq

Native ChIP was carried out in two biological replicates following the published protocol with minor changes (Kelly et al., 2018). In brief, cell pellets (P19 EC cells-derived NSPCs and digested telencephalon cells at E13.5 and E16.5) were resuspended in 500 μL swollen buffer (0.3 M sucrose, 60 mM KCl, 15 mM NaCl, 5 mM MgCl$_2$, 0.1 mM EDTA, 15 mM Tris-HCl [pH 7.5], 5 mM sodium butyrate, and 1× protease inhibitor cocktail). Nuclei were isolated using an equal volume extraction buffer (0.3 M sucrose, 60 mM KCl, 15 mM NaCl, 5 mM MgCl$_2$, 0.1 mM EDTA, 15

mM Tris-HCl [pH 7.5], 0.4 % NP-40, 5 mM sodium butyrate, and 1× protease inhibitor cocktail) with gentle rotation (30 rpm) at 4°C for 10 min. The cell suspensions were transferred into new tubes containing 500 µL sucrose cushion buffer (0.6 M sucrose, 60 mM KCl, 15 mM NaCl, 5 mM MgCl$_2$, 0.1 mM EDTA, 15 mM Tris-HCl [pH 7.5], 5 mM sodium butyrate, and 1× protease inhibitor cocktail) and centrifuge at 1500 g for 10 min at 4°C. Nuclei were softly resuspended by MNase digestion buffer (0.32 M sucrose, 4 mM MgCl$_2$, 1 mM CaCl$_2$, 50 mM Tris-HCl [pH 7.5], 5 mM sodium butyrate, and 1× protease inhibitor cocktail). The amount of chromatin present in the sample was assessed by spectrophotometry in the presence of 0.1% SDS, and chromatin was then digested using Micrococcal nuclease (Takara) (1 U per 10 µg chromatin) at 600 rpm in a thermomixer for 5 min at 37°C. The reaction was stopped by adding EDTA to a final concentration of 5 mM and incubated on ice for 5 min, then cleared at 12,000 g for 10 min at 4°C. The supernatant (S1 fraction) was stored at 4°C and the pellets were resuspended in dialysis buffer (0.2 mM EDTA, 1 mM Tris-HCl [pH 7.5], and 5 mM sodium butyrate), and then dialyze against 1.5 L dialysis buffer by Slide-A-Lyzer Dialysis Cassettes, 10K MWCO, 3 mL (Thermo Scientific) overnight at 4°C. The dialyzed pellets (S2 fraction) were cleared at 20,000 g for 10 min at 4°C and combined with S1 fraction for immunoprecipitation.

Exceptionally, we measured the dsDNA amount of the combined S1 and S2 fractions using Qubit 4.0 fluorometer (Invitrogen) by Equalbit 1 × dsDNA HS Assay Kit (Vazyme) to enable an accurate calculation of the chromatin amount used for immunoprecipitation experiments. Finally, 25 µg chromatin (dsDNA) was immunoprecipitated using 1.25 µg H3K9ac (PTM Biolabs, Hangzhou, China) and H3K9cr (PTM Biolabs), and 150 µg chromatin was immunoprecipitated using 3 µg H3K18la (PTM Biolabs) overnight at 4°C with gentle rotation (20 rpm) in ChIP dilution buffer (1% Triton X-100, 2 mM EDTA, 150 mM NaCl, 50 mM Tri-HCl [pH 7.5], 5 mM sodium butyrate, and 1× protease inhibitor cocktail). Antibodies-chromatin complexes were collected using 20 µL Magna ChIP protein A + G magnetic beads (Millipore) by incubation with rotation (20 rpm) for 2 h at 4°C, and the beads were sequentially washed once with low salt wash buffer (0.1% SDS, 1%

Triton X-100, 2 mM EDTA, 150 mM NaCl, and 20 mM Tris-HCl [pH 8.1]), once with high salt wash buffer (0.1% SDS, 1% Triton X-100, 2 mM EDTA, 500 mM NaCl, and 20 mM Tris-HCl [pH 8.1]), once with LiCl wash buffer (250 mM LiCl, 1% NP-40, 10 mM Tris-HCl [pH 8.1], 1% sodium deoxycholate, and 1 mM EDTA), and twice with TE buffer (10 mM Tris-HCl [pH 8.1] and 1 mM EDTA) for 10 min each at 4°C and 30 rpm. Immune complexes were eluted from the beads twice for 15 min at 65°C and 1000 rpm in a thermomixer using 250 μL elution buffer (1% SDS and 100 mM NaHCO$_3$). The eluted immune complexes were then treated with RNase A (100 μg/ml) for 30 min at 37°C, and followed by Proteinase K (50 μg/ml) for 2 h at 58°C and 600 rpm in a thermomixer. Then, the IPed DNA was purified using the phenol-chloroform-isoamyl alcohol (25:24:1) and precipitated with two volumes of 100% ethanol and 10 ug linear acrylamide (Invitrogen) at -20°C for 2h. Libraries were then constructed with the TruSeq ChIP Library Preparation Kit (Illumina) following the manufacturer's instructions and sequenced on Illumina platforms by Annoroad Gene Technology Co., Ltd.

Sequencing data filtering

The original image data obtained after sequencing was converted into the sequence data stored in FASTQ file format by base calling. The raw reads of the datasets were filtered by Trimmomatic (v0.36) to remove contaminations and low-quality reads with the parameters "ILLUMINACLIP:Adapter.fa:2:30:10 SLIDINGWINDOW:4:15 LEADING:3 TRAILING:3 MINLEN:36" and quality-controlled using FastQC (v0.11.7) (Bolger et al., 2014).

ATAC-seq data analysis

The reads of ATAC-seq data were aligned using Bowtie 2 (v2.4.1) to the mouse reference genome with parameters "-X 1000 --mm --local" (Langmead and Salzberg, 2012). Samtools (v1.10) was then used to convert files into bam format and filter

mapped reads with parameters "-F 1804 -f 2 -q 30" (Li et al., 2009). Next, we removed PCR duplicates using Mark Duplicates function in Picard (v2.22.0) and mitochondrial reads. Finally, MACS2 (v2.2.7.1) was used to call peaks with parameters "--keep-dup all -q 0.01 -f BAMPE" (Li et al., 2009). The quality control of ATAC-seq data is shown in Table S3.

ChIP-seq data analysis

High-quality ChIP-seq reads were aligned using Bowtie 2 to the mouse reference genome using default parameters. Samtools was used to convert files into bam format and filter mapped reads with parameters "-F 1804 -f 2 -q 30". PCR duplicates were removed using the Mark Duplicates function in Picard, and MACS2 was used to perform peak calling (-q 0.01) for the IP samples relative to the input samples. The quality control of ChIP-seq data is shown in Table S3.

RNA-seq data analysis

High-quality reads of RNA-seq data were quantified using Salmon (v1.1.0) with parameters "-i -g --gcBias --validateMappings" (Patro et al., 2017). Differential gene expression analysis was conducted using DESeq2 (v1.26.0) and differentially expressed genes were defined by P-adjust < 0.05, and absolute fold change more than 0 (Love et al., 2014). The quality control of RNA-seq data is shown in Table S3.

Peak annotation and gene enrichment analysis

Peak annotation was performed using ChIPseeker (v1.22.1) at gene level and promoter regions was defined as ± 2 kb of TSS (Yu et al., 2015). Genes were considered under regulation of histone marks with at least one peak annotated in their promoter regions or gene body regions. Gene enrichment analysis was performed using clusterProfiler (v3.14.3) with default parameters (Yu et al., 2012).

Quantitative comparison of ChIP-seq data

To analyze dynamic changes in histone acylations at promoter regions, the BEDTools (v2.29.0) "coverage" function was used for read counting within ± 2 kb of TSS (Quinlan and Hall, 2010), and DESeq2 was then used to perform quantitative analysis of genes with differential histone acylations which were defined by P-adjust < 0.05, and absolute fold change more than 1.5. DiffBind (v2.14.0) and MAnorm (v1.2.0) were adopted to perform analysis of dynamic changes in histone acylations at peak regions, and peaks with differential histone acylations were defined by P-adjust < 0.05, and absolute fold change more than 1.5 (Shao et al., 2012). Genes with differential histone acylations were defined as at least one peak annotated in their promoter regions or gene body regions. For comparison analysis of histone acylations enrichment among different groups of NSPCs, BEDTools "coverage" function was used for read counting within both ± 2 kb of TSS (promoter regions) and gene body regions, then the raw read counts were used to calculate reads per kilobase per million mapped reads (RPKM) values to represent ChIP signals as follows: [(read counts) / (region length in kb)] / (total mapped and filtered reads in Mb).

Sequencing data visualization

Bam files were converted into bigwig files using deepTools (v3.4.0) "bamCoverage" function with parameters "--binSize 50 --normalizeUsing RPKM", and "computeMatrix," "plotHeatmap," "multiBigwigSummary" and "plotCorrelation" functions were used to generate heatmaps (Ramírez et al., 2016). For genome browser representation, data in bigwig files generated by deepTools were visualized using IGV (v. 2.4.10) (Thorvaldsdóttir et al., 2013). BETA "basic" function (--df 0.05 --da 1 -c 0.001) was used for activating and repressive function prediction of peak regions with differential histone acylations (Wang et al., 2013). Peaks between replicates were combined by BEDtools "intersect" function, and bigwig files between replicates were merged by deepTools "bigwigCompare" functions with parameters "--operation

mean". The mouse reference genome sequence (vM24) and gene annotation (vM24) were downloaded from GENCODE (https://www.gencodegenes.org/).

Statistical analysis

The results shown are the mean ± SEM. One-way ANOVA with post hoc Tukey's test, unpaired two-tailed Student's t test, Kruskal-Wallis with post hoc Dunn's test, unpaired two-tailed Student's t test with Welch's correction, and two-sided Fisher's exact test were used to analyze statistical significance. Differences were regarded as significant by P value; NS: no significance, $*P < 0.05$, $**P < 0.01$, and $***P < 0.001$. All statistical analysis and diagrams were performed using GraphPad Prism 8.0 and R (v3.6.3). Statistical details and methods used in each experiment can be found in the respective figure legends.

Competing of interests

The authors declare no competing or financial interests.

Author contributions

Conceptualization: S.K.D, C.M.L.; Design and analysis of experiments: S.K.D., X.L., L.F.J., P.P.L.; Writing - original Draft: S.K.D.; Writing - review & editing: S.K.D., C.M.L., Q.Z.T.; Supervision: C.M.L., Q.Z.T...

Data availability

The ATAC-seq, ChIP-seq, and RNA-seq datasets generated and analyzed during the current study have been deposited in the NCBI Gene Expression Omnibus (GEO) and are accessible through the series accession numbers GSE171088 and GSE171832. Sequence tracks of our study are displayed in UCSC genome browser through session "Histone_Kcr_Kla" (https://genome.ucsc.edu/s/DaiSK/Histone_Kcr_Kla).

(https://www.ncbi.nlm.nih.gov/geo/query/acc.cgi?acc=GSE171088, secure token for reviewer access: otideiqevbyfvub) for GSE171088.

(https://www.ncbi.nlm.nih.gov/geo/query/acc.cgi?acc=GSE171832, secure token for reviewer access: mlonosimhrmltyx) for GSE171832.

References

Andrews, F. H., Shinsky, S. A., Shanle, E. K., Bridgers, J. B., Gest, A., Tsun, I. K., Krajewski, K., Shi, X., Strahl, B. D. and Kutateladze, T. G. (2016). The Taf14 YEATS domain is a reader of histone crotonylation. *Nat. Chem. Biol.* **12**, 396-398.

Bensaude, O. (2011). Inhibiting eukaryotic transcription: Which compound to choose? How to evaluate its activity? *Transcription* **2**, 103-108.

Bolger, A. M., Lohse, M. and Usadel, B. (2014). Trimmomatic: a flexible trimmer for Illumina sequence data. *Bioinformatics (Oxford, England)* **30**, 2114-2120.

Crespo, M., Damont, A., Blanco, M., Lastrucci, E., Kennani, S. E., Ialy-Radio, C., Khattabi, L. E., Terrier, S., Louwagie, M., Kieffer-Jaquinod, S., et al. (2020). Multi-omic analysis of gametogenesis reveals a novel signature at the promoters and distal enhancers of active genes. *Nucleic Acids Res.* **48**, 4115-4138.

Dai, S. K., Liu, P. P., Du, H. Z., Liu, X., Xu, Y. J., Liu, C., Wang, Y. Y., Teng, Z. Q. and Liu, C. M. (2021). Histone crotonylation regulates neural stem cell fate decisions by activating bivalent promoters. *EMBO Rep.* **22**, e52023.

Diehl, K. L. and Muir, T. W. (2020). Chromatin as a key consumer in the metabolite economy. *Nat. Chem. Biol.* **16**, 620-629.

Fang, Y., Xu, X., Ding, J., Yang, L., Doan, M. T., Karmaus, P. W. F., Snyder, N. W., Zhao, Y., Li, J. L. and Li, X. (2021). Histone crotonylation promotes mesoendodermal commitment of human embryonic stem cells. *Cell stem cell* **28**, 748-763.e747.

Fellows, R., Denizot, J., Stellato, C., Cuomo, A., Jain, P., Stoyanova, E., Balázsi, S., Hajnády, Z., Liebert, A., Kazakevych, J., et al. (2018). Microbiota derived short chain fatty acids promote histone crotonylation in the colon through histone deacetylases. *Nat. Commun.* **9**, 105.

Gowans, G. J., Bridgers, J. B., Zhang, J., Dronamraju, R., Burnetti, A., King, D. A., Thiengmany, A. V., Shinsky, S. A., Bhanu, N. V., Garcia, B. A., et al. (2019). Recognition of Histone Crotonylation by Taf14 Links Metabolic State to Gene Expression. *Mol. Cell* **76**, 909-921.e903.

Huang, H., Zhang, D., Wang, Y., Perez-Neut, M., Han, Z., Zheng, Y. G., Hao, Q. and Zhao, Y. (2018). Lysine benzoylation is a histone mark regulated by SIRT2. *Nat. Commun.* **9**, 3374.

Huang, H., Zhang, D., Weng, Y., Delaney, K., Tang, Z., Yan, C., Qi, S., Peng, C., Cole, P. A., Roeder, R. G., et al. (2021). The regulatory enzymes and protein substrates for the lysine β-hydroxybutyrylation pathway. *Sci. Adv.* **7**, eabe2771.

Jiang, G., Nguyen, D., Archin, N. M., Yukl, S. A., Méndez-Lagares, G., Tang, Y., Elsheikh, M. M., Thompson, G. R., 3rd, Hartigan-O'Connor, D. J., Margolis, D. M., et al. (2018). HIV latency is reversed by ACSS2-driven histone crotonylation. *J. Clin. Invest.* **128**, 1190-1198.

Kelly, R. D. W., Chandru, A., Watson, P. J., Song, Y., Blades, M., Robertson, N. S., Jamieson, A. G., Schwabe, J. W. R. and Cowley, S. M. (2018). Histone deacetylase (HDAC) 1 and 2 complexes regulate both histone acetylation and crotonylation in vivo. *Sci. Rep.* **8**, 14690.

Khacho, M., Harris, R. and Slack, R. S. (2019). Mitochondria as central regulators of neural stem cell fate and cognitive function. *Nat. Rev. Neurosci.* **20**, 34-48.

Klemm, S. L., Shipony, Z. and Greenleaf, W. J. (2019). Chromatin accessibility and the regulatory epigenome. *Nat. Rev. Genet.* **20**, 207-220.

Kollenstart, L., de Groot, A. J. L., Janssen, G. M. C., Cheng, X., Vreeken, K., Martino, F., Côté, J., van Veelen, P. A. and van Attikum, H. (2019). Gcn5 and Esa1 function as histone crotonyltransferases to regulate crotonylation-dependent transcription. *J. Biol. Chem.* **294**, 20122-20134.

Langmead, B. and Salzberg, S. L. (2012). Fast gapped-read alignment with Bowtie 2. *Nat. Methods* **9**, 357-359.

Li, H., Handsaker, B., Wysoker, A., Fennell, T., Ruan, J., Homer, N., Marth, G., Abecasis, G. and Durbin, R. (2009). The Sequence Alignment/Map format and SAMtools. *Bioinformatics (Oxford, England)* **25**, 2078-2079.

Li, K. and Wang, Z. (2021). Histone crotonylation-centric gene regulation. *Epigenetics & chromatin* **14**, 10.

Li, L., Chen, K., Wang, T., Wu, Y., Xing, G., Chen, M., Hao, Z., Zhang, C., Zhang, J., Ma, B., et al. (2020). Glis1 facilitates induction of pluripotency via an epigenome-metabolome-epigenome signalling cascade. *Nat. Metab.* **2**, 882-892.

Li, L., Jin, J. and Yang, X. J. (2019). Histone Deacetylase 3 Governs Perinatal Cerebral Development via Neural Stem and Progenitor Cells. *iScience* **20**, 148-167.

Li, X., Egervari, G., Wang, Y., Berger, S. L. and Lu, Z. (2018). Regulation of chromatin and gene expression by metabolic enzymes and metabolites. *Nat. Rev. Mol. Cell Biol.* **19**, 563-578.

Li, Y., Sabari, B. R., Panchenko, T., Wen, H., Zhao, D., Guan, H., Wan, L., Huang, H., Tang, Z., Zhao, Y., et al. (2016). Molecular Coupling of Histone Crotonylation and Active Transcription by AF9 YEATS Domain. *Mol. Cell* **62**, 181-193.

Li, Y., Wen, H., Xi, Y., Tanaka, K., Wang, H., Peng, D., Ren, Y., Jin, Q., Dent, S. Y., Li, W., et al. (2014). AF9 YEATS domain links histone acetylation to DOT1L-mediated H3K79 methylation. *Cell* **159**, 558-571.

Lipinski, M., Muñoz-Viana, R., Del Blanco, B., Marquez-Galera, A., Medrano-Relinque, J., Caramés, J. M., Szczepankiewicz, A. A., Fernandez-Albert, J., Navarrón, C. M., Olivares, R., et al. (2020). KAT3-dependent acetylation of cell type-specific genes maintains neuronal identity in the adult mouse brain. *Nat. Commun.* **11**, 2588.

Liu, J., Wu, X., Zhang, H., Pfeifer, G. P. and Lu, Q. (2017a). Dynamics of RNA Polymerase II Pausing and Bivalent Histone H3 Methylation during Neuronal Differentiation in Brain Development. *Cell Rep.* **20**, 1307-1318.

Liu, S., Yu, H., Liu, Y., Liu, X., Zhang, Y., Bu, C., Yuan, S., Chen, Z., Xie, G., Li, W., et al. (2017b). Chromodomain Protein CDYL Acts as a Crotonyl-CoA Hydratase to Regulate Histone Crotonylation and Spermatogenesis. *Mol. Cell* **67**, 853-866.e855.

Liu, X., Wei, W., Liu, Y., Yang, X., Wu, J., Zhang, Y., Zhang, Q., Shi, T., Du, J. X., Zhao, Y., et al. (2017c). MOF as an evolutionarily conserved histone crotonyltransferase and transcriptional activation by histone acetyltransferase-deficient and crotonyltransferase-competent CBP/p300. *Cell Discov.* **3**, 17016.

Liu, Y., Li, M., Fan, M., Song, Y., Yu, H., Zhi, X., Xiao, K., Lai, S., Zhang, J., Jin, X., et al. (2019). Chromodomain Y-like Protein-Mediated Histone Crotonylation Regulates Stress-Induced Depressive Behaviors. *Biol. Psychiatry* **85**, 635-649.

Love, M. I., Huber, W. and Anders, S. (2014). Moderated estimation of fold change and dispersion for RNA-seq data with DESeq2. *Genome Biol.* **15**, 550.

Lu, Y., Xu, Q., Liu, Y., Yu, Y., Cheng, Z. Y., Zhao, Y. and Zhou, D. X. (2018). Dynamics and functional interplay of histone lysine butyrylation, crotonylation, and acetylation in rice under starvation and submergence. *Genome Biol.* **19**, 144.

Luo, Z., Lin, C. and Shilatifard, A. (2012). The super elongation complex (SEC) family in transcriptional control. *Nat. Rev. Mol. Cell Biol.* **13**, 543-547.

Martin, B. J. E., Brind'Amour, J., Kuzmin, A., Jensen, K. N., Liu, Z. C., Lorincz, M. and Howe, L. J. (2021). Transcription shapes genome-wide histone acetylation patterns. *Nat. Commun.* **12**, 210.

Marzluff, W. F. and Koreski, K. P. (2017). Birth and Death of Histone mRNAs. *Trends Genet.* **33**, 745-759.

Moreno-Yruela, C., Zhang, D., Wei, W., Baek, M., Gao, J. J., Nielsen, A. L., Bolding, J. E., Yang, L., Jameson, S. T., Wong, J. M., et al. (2021). Class I Histone Deacetylases (HDAC1–3) are Histone Lysine Delactylases. *BioRxiv*.

Patro, R., Duggal, G., Love, M. I., Irizarry, R. A. and Kingsford, C. (2017). Salmon provides fast and bias-aware quantification of transcript expression. *Nat. Methods* **14**, 417-419.

Quinlan, A. R. and Hall, I. M. (2010). BEDTools: a flexible suite of utilities for comparing genomic features. *Bioinformatics (Oxford, England)* **26**, 841-842.

Ramírez, F., Ryan, D. P., Grüning, B., Bhardwaj, V., Kilpert, F., Richter, A. S., Heyne, S., Dündar, F. and Manke, T. (2016). deepTools2: a next generation web server for deep-sequencing data analysis. *Nucleic Acids Res.* **44**, W160-165.

Sabari, B. R., Tang, Z., Huang, H., Yong-Gonzalez, V., Molina, H., Kong, H. E., Dai, L., Shimada, M., Cross, J. R., Zhao, Y., et al. (2015). Intracellular crotonyl-CoA stimulates transcription through p300-catalyzed histone crotonylation. *Mol. Cell* **58**, 203-215.

Shao, Z., Zhang, Y., Yuan, G. C., Orkin, S. H. and Waxman, D. J. (2012). MAnorm: a robust model for quantitative comparison of ChIP-Seq data sets. *Genome Biol.* **13**, R16.

Shechter, D., Dormann, H. L., Allis, C. D. and Hake, S. B. (2007). Extraction, purification and analysis of histones. *Nat. Protoc.* **2**, 1445-1457.

Tan, M., Luo, H., Lee, S., Jin, F., Yang, J. S., Montellier, E., Buchou, T., Cheng, Z., Rousseaux, S., Rajagopal, N., et al. (2011). Identification of 67 histone marks and histone lysine crotonylation as a new type of histone modification. *Cell* **146**, 1016-1028.

Tang, T., Zhang, Y., Wang, Y., Cai, Z., Lu, Z., Li, L., Huang, R., Hagelkruys, A., Matthias, P., Zhang, H., et al. (2019). HDAC1 and HDAC2 Regulate Intermediate Progenitor Positioning to Safeguard Neocortical Development. *Neuron* **101**, 1117-1133.e1115.

Tang, X., Chen, X. F., Sun, X., Xu, P., Zhao, X., Tong, Y., Wang, X. M., Yang, K., Zhu, Y. T., Hao, D. L., et al. (2021). Short-Chain Enoyl-CoA Hydratase Mediates Histone Crotonylation and Contributes to Cardiac Homeostasis. *Circulation* **143**, 1066-1069.

Thorvaldsdóttir, H., Robinson, J. T. and Mesirov, J. P. (2013). Integrative Genomics Viewer (IGV): high-performance genomics data visualization and exploration. *Brief. Bioinform.* **14**, 178-192.

Vaid, R., Wen, J. and Mannervik, M. (2020). Release of promoter-proximal paused Pol II in response to histone deacetylase inhibition. *Nucleic Acids Res.* **48**, 4877-4890.

Wang, J., Weaver, I. C., Gauthier-Fisher, A., Wang, H., He, L., Yeomans, J., Wondisford, F., Kaplan, D. R. and Miller, F. D. (2010). CBP histone acetyltransferase activity regulates embryonic neural differentiation in the normal and Rubinstein-Taybi syndrome brain. *Dev. Cell* **18**, 114-125.

Wang, S., Sun, H., Ma, J., Zang, C., Wang, C., Wang, J., Tang, Q., Meyer, C. A., Zhang, Y. and Liu, X. S. (2013). Target analysis by integration of transcriptome and ChIP-seq data with BETA. *Nat. Protoc.* **8**, 2502-2515.

Wang, Z., Zang, C., Cui, K., Schones, D. E., Barski, A., Peng, W. and Zhao, K. (2009). Genome-wide mapping of HATs and HDACs reveals distinct functions in active and inactive genes. *Cell* **138**, 1019-1031.

Wei, W., Liu, X., Chen, J., Gao, S., Lu, L., Zhang, H., Ding, G., Wang, Z., Chen, Z., Shi, T., et al. (2017). Class I histone deacetylases are major histone decrotonylases: evidence for critical and broad function of histone crotonylation in transcription. *Cell Res.* **27**, 898-915.

Xiong, X., Panchenko, T., Yang, S., Zhao, S., Yan, P., Zhang, W., Xie, W., Li, Y., Zhao, Y., Allis, C. D., et al. (2016). Selective recognition of histone crotonylation by double PHD fingers of MOZ and DPF2. *Nat. Chem. Biol.* **12**, 1111-1118.

Yao, B., Christian, K. M., He, C., Jin, P., Ming, G. L. and Song, H. (2016). Epigenetic mechanisms in neurogenesis. *Nat. Rev. Neurosci.* **17**, 537-549.

Yu, G., Wang, L. G., Han, Y. and He, Q. Y. (2012). clusterProfiler: an R package for comparing biological themes among gene clusters. *Omics.* **16**, 284-287.

Yu, G., Wang, L. G. and He, Q. Y. (2015). ChIPseeker: an R/Bioconductor package for ChIP peak annotation, comparison and visualization. *Bioinformatics (Oxford, England)* **31**, 2382-2383.

Yu, J., Chai, P., Xie, M., Ge, S., Ruan, J., Fan, X. and Jia, R. (2021). Histone lactylation drives oncogenesis by facilitating m(6)A reader protein YTHDF2 expression in ocular melanoma. *Genome Biol.* **22**, 85.

Zhang, D., Tang, Z., Huang, H., Zhou, G., Cui, C., Weng, Y., Liu, W., Kim, S., Lee, S., Perez-Neut, M., et al. (2019). Metabolic regulation of gene expression by histone lactylation. *Nature* **574**, 575-580.

Zhao, D., Guan, H., Zhao, S., Mi, W., Wen, H., Li, Y., Zhao, Y., Allis, C. D., Shi, X. and Li, H. (2016). YEATS2 is a selective histone crotonylation reader. *Cell Res.* **26**, 629-632.

Figures

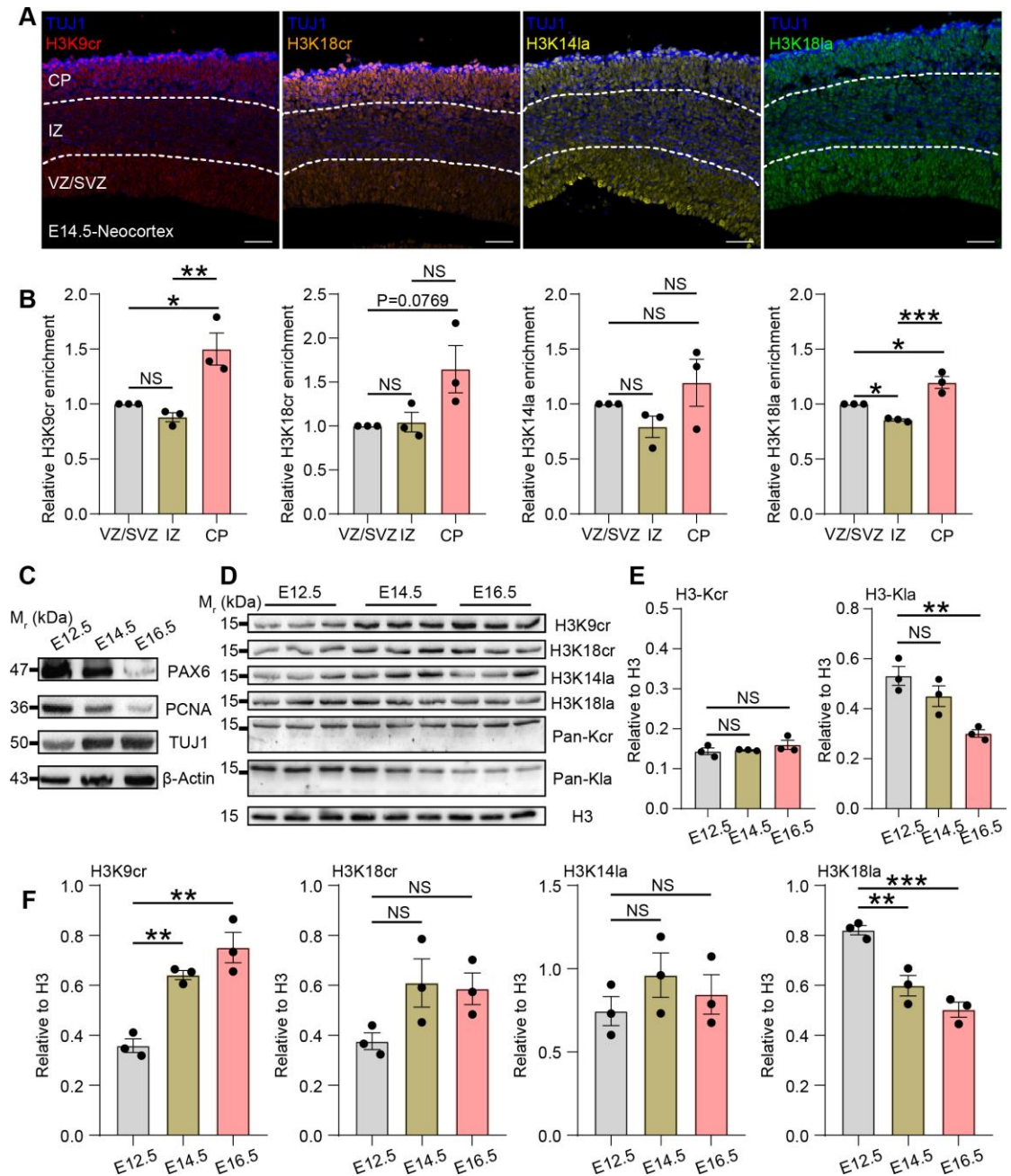**Fig. 1. Existence and changes of histone Kcr and Kla during neural development.**
(A) Immunostaining results of H3K9cr, H3K18cr, H3K14la, and H3K18la on the mouse forebrain sections at E14.5 ($n = 1$ embryonic mice). Scale bar, 50 μm. VZ/SVZ: ventricular/subventricular zone, IZ: intermediate zone, and CP: cortical plate. (B) Quantitative analysis of enrichment levels of H3K9cr, H3K18cr, H3K14la, and

H3K18la across the layers of E14.5 cortex. Data are presented as mean ± SEM of three independent biological replicates, $n = 3$. One-way ANOVA with post hoc Tukey's test was used to analyze statistical significance; NS: no significance, $^{*}P < 0.05$, $^{**}P < 0.01$, and $^{***}P < 0.001$. (C) Western blot assay showing changes in PAX6, PCNA, and TUJ1 levels in the developing telencephalon. (D) Western blot assay showing changes in H3K9cr, H3K18cr, H3K14la, H3K18la, H3-Kcr, and H3-Kla levels in the developing telencephalon. (E) Quantitative analysis of changes in H3-Kcr and H3-Kla levels in the developing telencephalon. Data are presented as mean ± SEM of three independent biological replicates, $n = 3$. One-way ANOVA with post hoc Tukey's test was used to analyze statistical significance; NS: no significance, $^{**}P < 0.01$. (F) Quantitative analysis of changes in H3K9cr, H3K18cr, H3K14la, and H3K18la levels in the developing telencephalon. Data are presented as mean ± SEM of three independent biological replicates, $n = 3$. One-way ANOVA with post hoc Tukey's test was used to analyze statistical significance; NS: no significance, $^{**}P < 0.01$, $^{***}P <0.001$.

A

H3K9ac
- Promoter (47.82%)
- 5' UTR (4.29%)
- 3' UTR (1.79%)
- Exon (3.96%)
- Intron (23.27%)
- Intergenic (18.87%)

H3K9cr
- Promoter (54.65%)
- 5' UTR (4.95%)
- 3' UTR (1.61%)
- Exon (3.58%)
- Intron (18.73%)
- Intergenic (16.48%)

H3K18la
- Promoter (26.88%)
- 5' UTR (2.01%)
- 3' UTR (1.5%)
- Exon (3.82%)
- Intron (33.89%)
- Intergenic (31.9%)

B

H3K9ac   H3K9cr   H3K18la   Chromatin accessibility   Gene expression

Gene count
4679
7773
42878

0 80   0 140   0 16   0 17.5   -4 4

C

Chromatin accessibility ***

$\log_2(\text{RPKM}+0.00001)$

Median: 0.8275, 0.8367, 0.8357, 0.9558

H3K9ac (13789) H3K9cr (13726) H3K18la (13113) Ac+Cr+La (10162)

Gene expression ***

$\log_{10}(\text{TPM}+0.00001)$

Median: 1.242, 1.246, 1.173, 1.371

H3K9ac (13789) H3K9cr (13726) H3K18la (13113) Ac+Cr+La (10162)

D

e.g. Cox5a, Sdhd, Sf3a1 — H3K9cr

Pathway	Gene count
Amyotrophic lateral sclerosis	125
Parkinson disease	94
Spliceosome	62
Ubiquitin mediated proteolysis	65
Alzheimer disease	121
Pathways of neurodegeneration - multiple diseases	144
Huntington disease	101
Prion disease	92
Protein processing in endoplasmic reticulum	67
mRNA surveillance pathway	47

$-\log_{10}(\text{p.adjust})$ 0 ... 15

e.g. Raf1, Bbc3, Cdkn1b — H3K18la

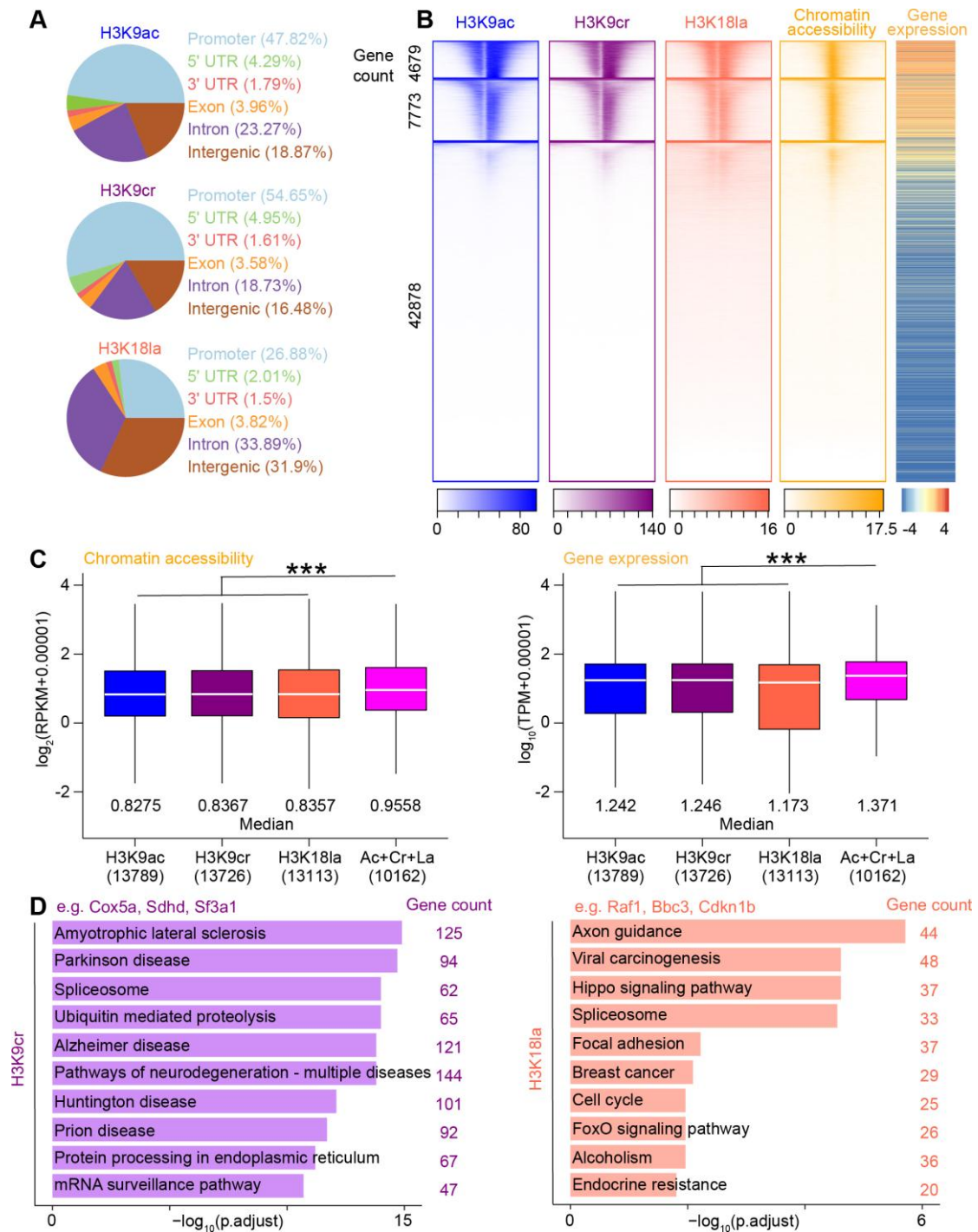| Pathway	Gene count
Axon guidance	44
Viral carcinogenesis	48
Hippo signaling pathway	37
Spliceosome	33
Focal adhesion	37
Breast cancer	29
Cell cycle	25
FoxO signaling pathway	26
Alcoholism	36
Endocrine resistance	20

$-\log_{10}(\text{p.adjust})$ 0 ... 6

Fig. 2. Multi-omics profiling and functional annotation of H3K9cr and H3K18la in vivo. (A) Pie charts showing the distribution of H3K9ac, H3K9cr, and H3K18la peaks in annotated genomic regions in the E13.5 telencephalon. (B) Density heatmaps in the E13.5 telencephalon for H3K9ac, H3K9cr, and H3K18la ChIP-seq and ATAC-seq at TSSs ± 2.5 kb of annotated genes, which were divided into three

clusters and ranked from the highest to the lowest by H3K9ac signal, with the number of genes in each cluster labeled on the left. The heatmap to the right of the density heatmaps displays expression levels (scaled by $\log_{10}$ [TPM+0.00001]) of genes ranked by decreasing H3K9ac signal. (C) Boxplots showing changes in chromatin accessibility levels (left panel) and expression levels (right panel) among different groups of genes in the E13.5 telencephalon. There were 13789, 13726, 13113, and 10162 genes under the regulation of H3K9ac, H3K9cr, H3K18la, and all three histone marks (Ac+Cr+La), respectively. The median for each dataset was noted below each boxplot. Kruskal-Wallis with post hoc Dunn's test was used to analyze statistical significance; ***P <0.001. (D) KEGG pathway enrichment analysis of genes under the regulation of H3K9cr (left panel, 3561 genes) and H3K18la (right panel, 3568 genes) in the E13.5 telencephalon.
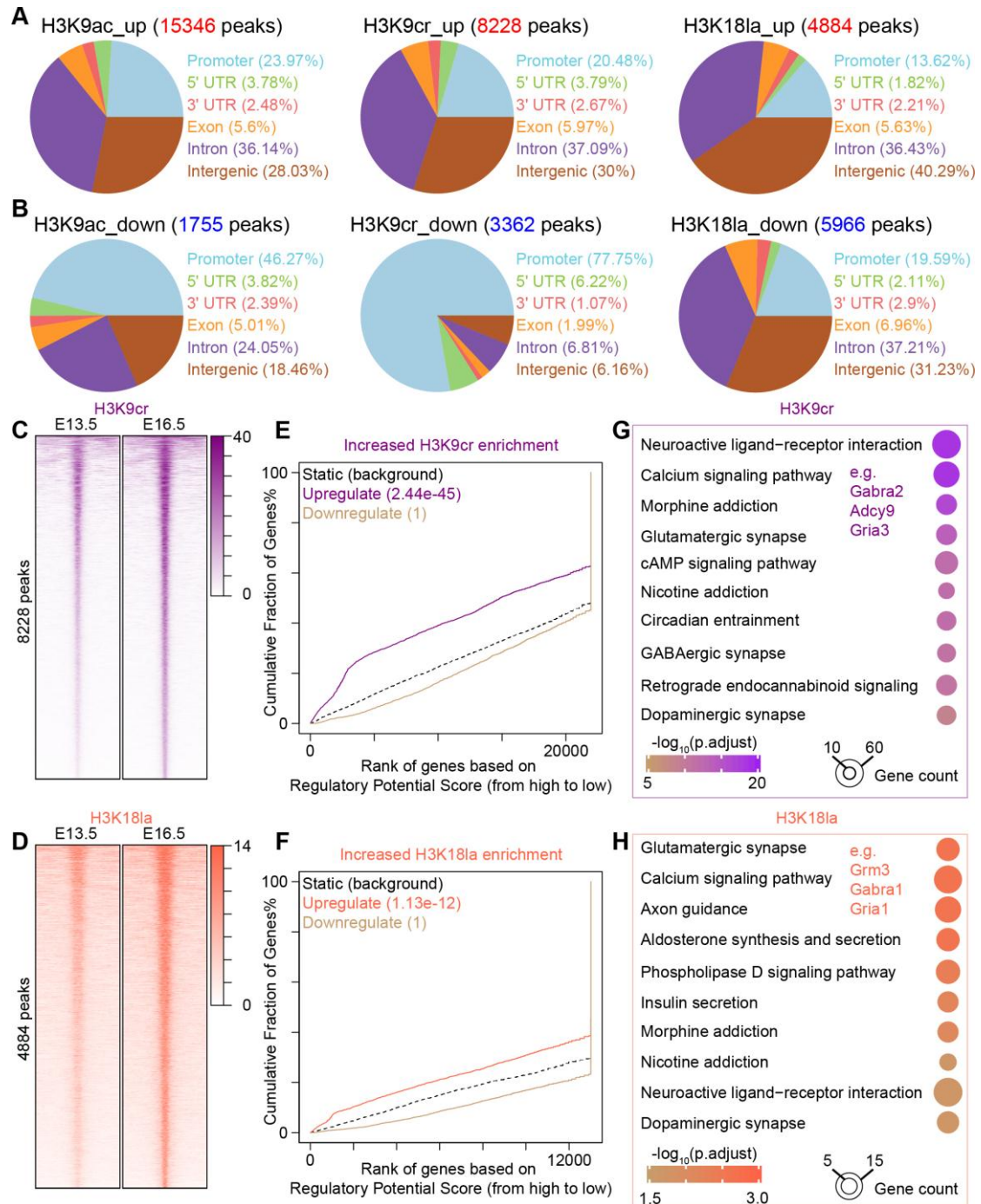
Fig. 3. Genome-wide changes in H3K9cr and H3K18la during neural development.

(A, B) Pie charts showing the distribution of peak regions with increased H3K9ac (A, left panel), H3K9cr (A, middle panel), and H3K18la (A, right panel), and reduced H3K9ac (B, left panel), H3K9cr (B, middle panel), and H3K18la (B, right panel) in annotated genomic regions during neural development, respectively. (C, D) Density

heatmaps in the developing telencephalon for H3K9cr (C) and H3K18la (D) ChIP-seq at ± 5 kb from the center of peak regions with increased H3K9cr (C) and H3K18la (D), respectively, and the number of peaks with differential histone acylations was labeled on the left. (E, F) BETA plot of combined computational analysis of ChIP-seq and RNA-seq data, peak regions with increased H3K9cr (E) and H3K18la (F) as input. (G, H) KEGG pathway enrichment analysis of upregulated genes with increased H3K9cr (G) and H3K18la (H) during neural development, there were 923 and 411 genes in (G) and (H), respectively.
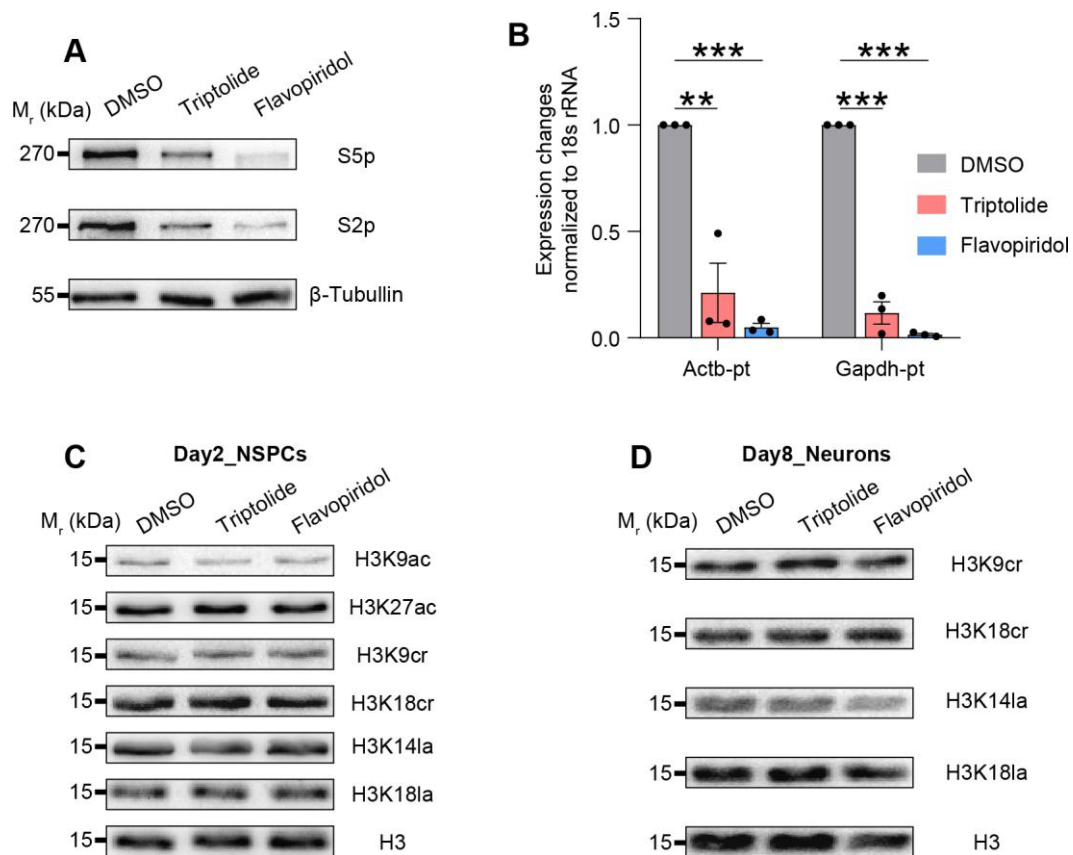
Fig. 4. The associations between transcription inhibition and histone Kcr and Kla levels. (A) Representative blots of changes in RNAP2 serine 5 CTD phosphorylation (S5p) and RNAP2 serine 2 CTD phosphorylation (S2p) levels among different treatments in P19 EC cells-derived NSPCs. (B) Quantification analysis of changes in nascent transcripts from the *Actb* and *Gapdh* genes among different treatments in P19 EC cells-derived NSPCs. Data are presented as mean ± SEM of three independent biological replicates, $n = 3$. Unpaired two-tailed Student's t test was used to analyze statistical significance; **P <0.01, ***P <0.001. (C, D) Representative blots of changes in indicated histone acylations levels among different treatments in P19 EC cells-derived NSPCs (C) and neurons (D).
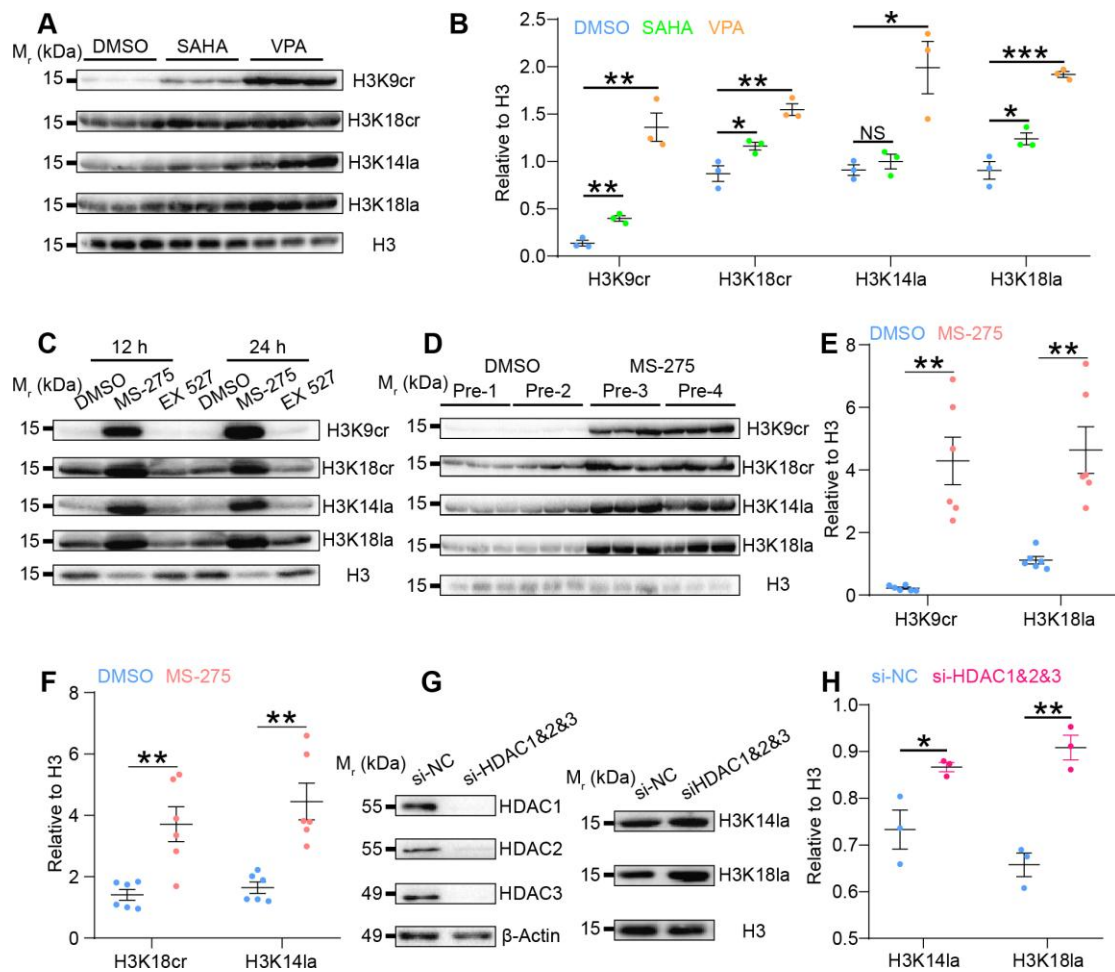
Fig. 5. HDAC1-3 inhibition stimulates histone Kcr and Kla levels. (A, B) Representative blots (A) and quantification analysis (B) of changes in H3K9cr, H3K18cr, H3K14la, and H3K18la levels among different treatments in P19 EC cells. Data are presented as mean ± SEM of three independent biological replicates, $n = 3$. Unpaired two-tailed Student's t test was used to analyze statistical significance; NS: no significance, $*P$ <0.05, $**P$ <0.01, and $***P$ <0.001. (C) Core histones were prepared from P19 EC cells treated with MS-275 and EX 527 for 12 h or 24 h and subjected to western blot assay using indicated antibodies, and the experiments were repeated once. (D–F) Representative blots (D) and quantification analysis (E and F) of changes in H3K9cr, H3K18cr, H3K14la, and H3K18la levels in the telencephalon at E15.5 injected with DMSO or MS-275 for two consecutive days (E13.5–E15.5), Pre: pregnant mice. Data are presented as mean ± SEM of six replicates from two independent biological replicates, $n = 6$. Unpaired two-tailed Student's t test with

Welch's correction was used to analyze statistical significance; **P <0.01. (G) Representative blots showing efficient knockdown of *Hdac1-3* (left panel) and changes in histone Kla levels (right panel) in P19 EC cells. (H) Quantification analysis of changes in H3K14la and H3K18la levels after *Hdac1-3* knockdown in P19 EC cells. Data are presented as mean ± SEM of three independent biological replicates, *n* = 3. Unpaired two-tailed Student's t test was used to analyze statistical significance; *P <0.05, **P <0.01.
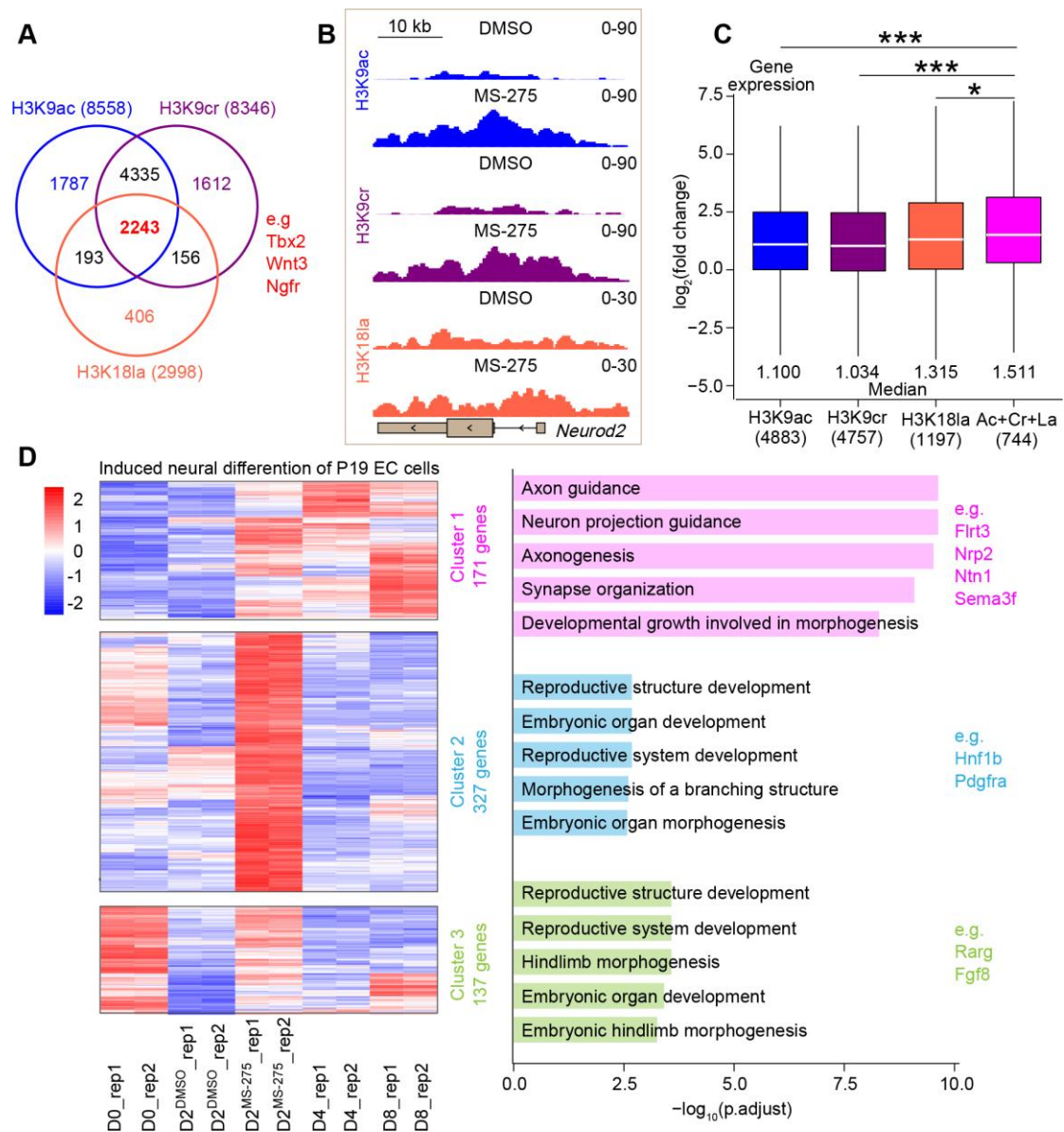
Fig. 6. HDAC1-3 regulates neural cell fate decisions by multiple histone acylations.

(A) Venn diagram of a combined comparison of groups of genes with increased H3K9ac, H3K9cr, and H3K18la after MS-275 treatment in P19 EC cells-derived NSPCs. (B) Genome-browser view at the *Neurod2* gene of different sequencing datasets. (C) Boxplots showing changes in expression levels among different groups of genes with increased histone acylations at their promoter regions after MS-275 treatment in P19 EC cells-derived NSPCs. There were 4883, 4757, 1197, and 744 genes with increased H3K9ac, H3K9cr, H3K18la, and all three histone marks

(Ac+Cr+La), respectively. The median for each dataset was noted below each boxplot. Kruskal-Wallis with post hoc Dunn's test was used to analyze statistical significance; *P <0.05, ***P <0.001. (D) Heatmap showing dynamic expression changes of upregulated genes (DESeq2 vsd-normalized RNA-seq counts and scaled by row) with increased H3K9ac, H3K9cr, and H3K18la after MS-275 treatment during neural differentiation process of P19 EC cells, and these genes were divided into three clusters according to their expression patterns (left panel), with the results of GO enrichment analysis (biological process) of genes in each cluster on the right panel.
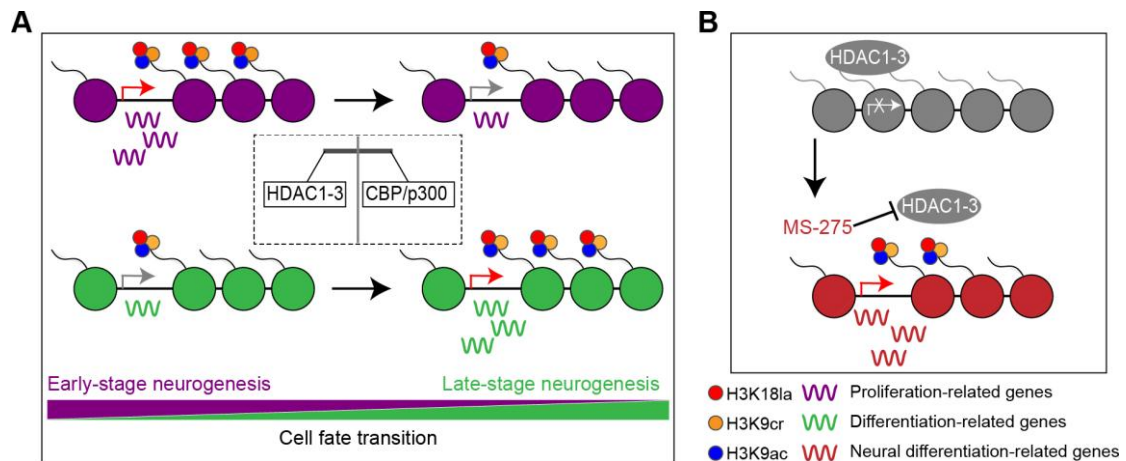
Fig. 7. Working models of multiple histone acylations to orchestrate gene expression in the neural system. (A) Genome-wide increase and reduce in H3K9ac, H3K9cr, and H3K18la are extensively involved in neuronal differentiation and cell proliferation processes, respectively, which orchestrate cell fate transitions during telencephalon development. (B) Inhibition of HDAC1-3 stimulates neural differentiation related transcriptional programs by multiple histone acylations including H3K9ac, H3K9cr, and H3K18la in the differentiating P19 EC cells.
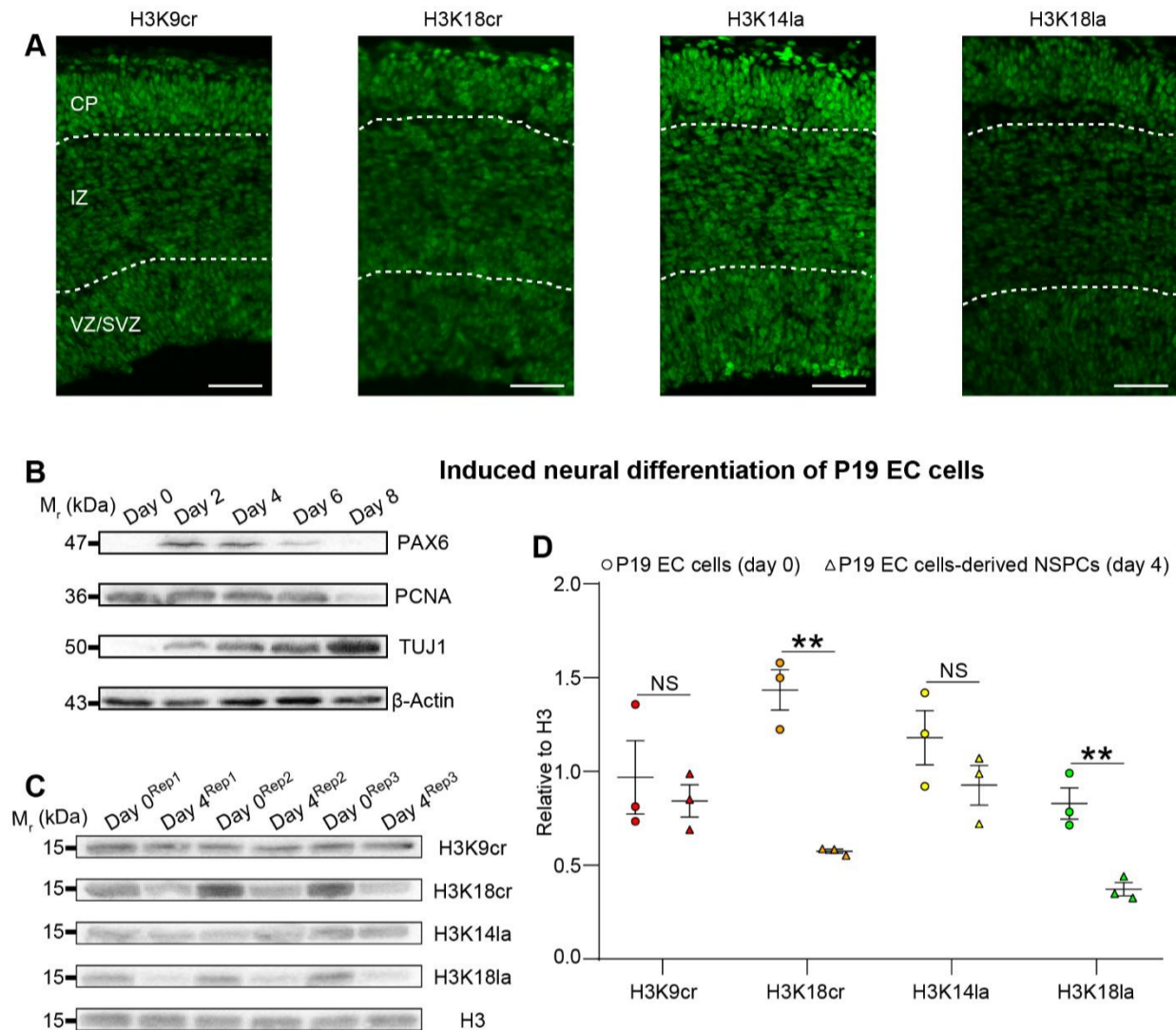
Fig. S1. Dynamic change of histone Kcr and Kla in vivo and in cells. (A) Representative images for enrichment levels of H3K9cr, H3K18cr, H3K14la, and H3K18la across the layers of E14.5 cortex. Scale bar, 50 μm. VZ/SVZ: ventricular/subventricular zone, IZ: intermediate zone, and CP: cortical plate. (B) Western blot assay showing changes in PAX6, PCNA, and TUJ1 levels across various time points of RA-induced neural differentiation of P19 EC cells. (C) Western blot assay showing changes in H3K9cr, H3K18cr, H3K14la, and H3K18la levels during induced neural differentiation of P19 EC cells. (D) Quantitative analysis of changes in H3K9cr, H3K18cr, H3K14la, and H3K18la levels during induced neural differentiation of P19 EC cells. Data are presented as mean ±SEM of three independent biological replicates, $n = 3$. Unpaired two-tailed Student's t test was used to analyze statistical significance; NS: no significance, $**$ $P < 0.01$.

A — H3K9ac, 1:500, catalog#: PTM-156, lot#: 212620242H316

Peptide samples (A):

1-1 H3K9ac 0.8 ng	2 H3K4cr-1 100 ng	6 H3K9me1 100 ng	10 H3K4cr-2 100 ng
1-2 H3K9ac 4 ng	3 H3K9bu 100 ng	7 H3K9me2 100 ng	11 H3K14ac 100 ng
1-3 H3K9ac 20 ng	4 H3K9hib 100 ng	8 H3K9cr 100 ng	12 H3K14cr 100 ng
1-4 H3K9ac 100 ng	5 H3K9bhb 100 ng	9 H3K4ac 100 ng	

B — H3K9cr, 1:10000, catalog#: PTM-516, lot#: ZD184J408P3

Peptide samples (B):

1-1 H3K9cr 1 ng	2-1 H3K14cr 1 ng	3-1 H3K27bu 1 ng	4-1 H3K27cr 1 ng	5-1 H3K18cr 1 ng	6 H3K9hib 64 ng	10 H3K27bhb 64 ng
1-2 H3K9cr 4 ng	2-2 H3K14cr 4 ng	3-2 H3K27bu 4 ng	4-2 H3K27cr 4 ng	5-2 H3K18cr 4 ng	7 H3K9bhb 64 ng	11 H3K4cr 64 ng
1-3 H3K9cr 16 ng	2-3 H3K14cr 16 ng	3-3 H3K27bu 16 ng	4-3 H3K27cr 16 ng	5-3 H3K18cr 16 ng	8 H3K9ac 64 ng	12 H3K9un 64 ng
1-4 H3K9cr 64 ng	2-4 H3K14cr 64 ng	3-4 H3K27bu 64 ng	4-4 H3K27cr 64 ng	5-4 H3K18cr 64 ng	9 H3K27hib 64 ng	

C — H3K18la, 1:2000, catalog#: PTM-1406, lot#: ZT599K825P8

Peptide samples (C):

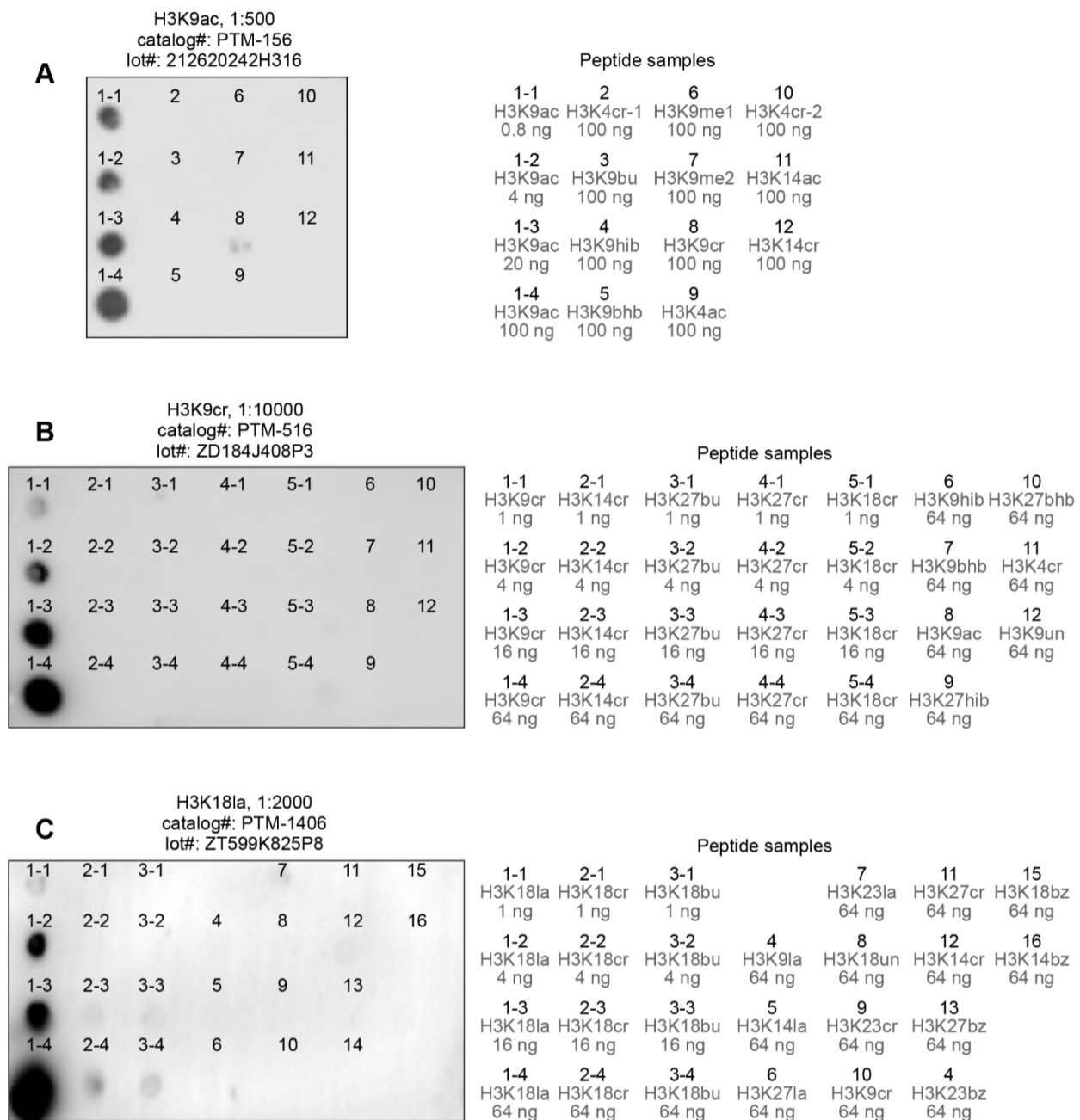|						
1-1 H3K18la 1 ng	2-1 H3K18cr 1 ng	3-1 H3K18bu 1 ng		7 H3K23la 64 ng	11 H3K27cr 64 ng	15 H3K18bz 64 ng
1-2 H3K18la 4 ng	2-2 H3K18cr 4 ng	3-2 H3K18bu 4 ng	4 H3K9la 64 ng	8 H3K18un 64 ng	12 H3K14cr 64 ng	16 H3K14bz 64 ng
1-3 H3K18la 16 ng	2-3 H3K18cr 16 ng	3-3 H3K18bu 16 ng	5 H3K14la 64 ng	9 H3K23bz 64 ng	13 H3K27bz 64 ng	
1-4 H3K18la 64 ng	2-4 H3K18cr 64 ng	3-4 H3K18bu 64 ng	6 H3K27la 64 ng	10 H3K9cr 64 ng	4 H3K23bz 64 ng	

Fig. S2. The specificity of the antibodies used in ChIP-seq assay. (A–C) Dot blot assay showing that the anti-H3K9ac, anti-H3K9cr, and anti-H3K18la antibodies are specific to H3K9ac (A), H3K9cr (B), and H3K18la (C), respectively, with information for peptides used on the right.
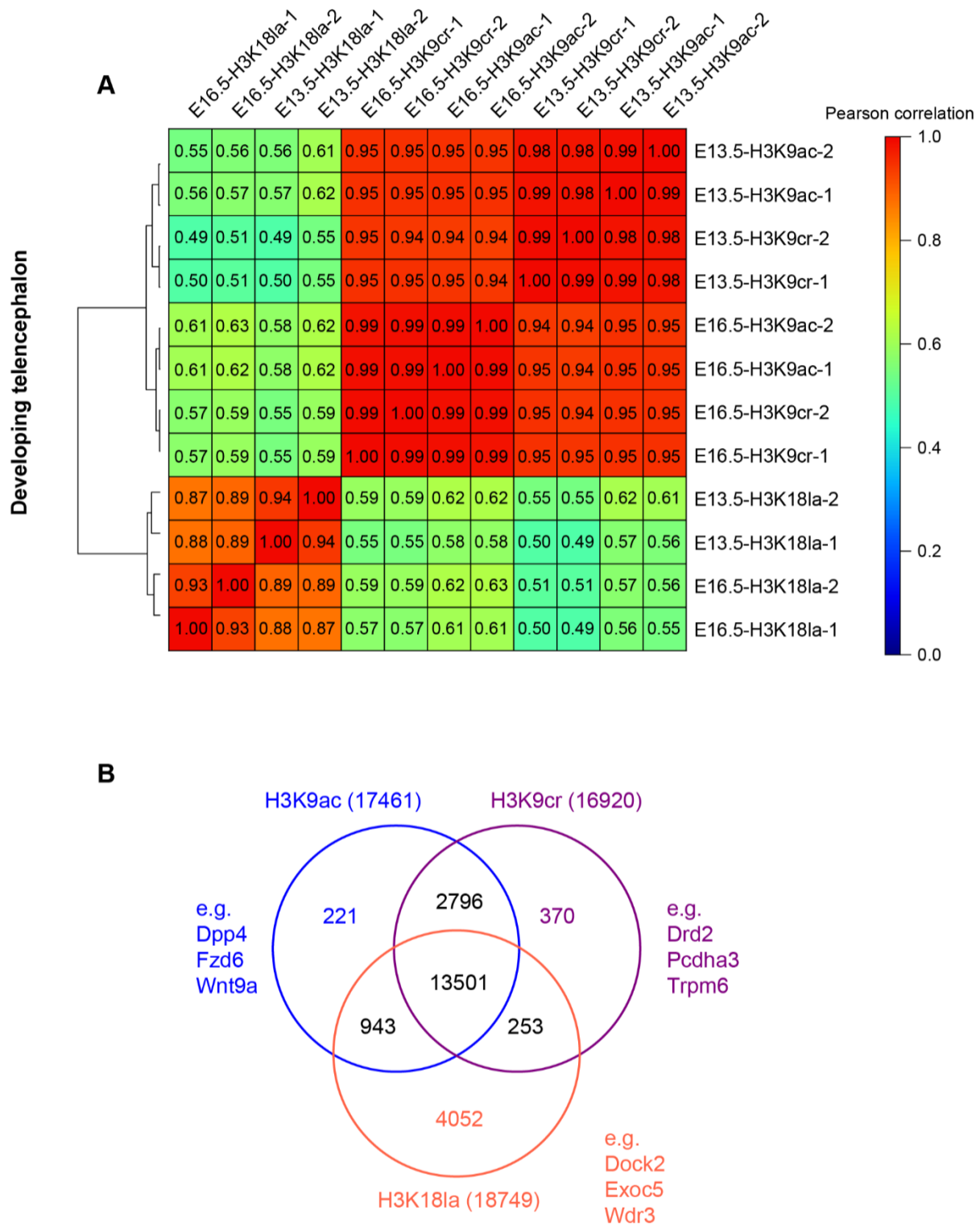
Fig. S3. The reproducibility and cluster analysis of ChIP-seq data. (A) The pearson correlation of ChIP-seq data among different developmental stages of the telencephalon. (B) Venn diagram of a combined comparison of groups of genes under the regulation of H3K9ac (17461 genes), H3K9cr (16920 genes), and H3K18la (18749 genes) in the E13.5 telencephalon, respectively.
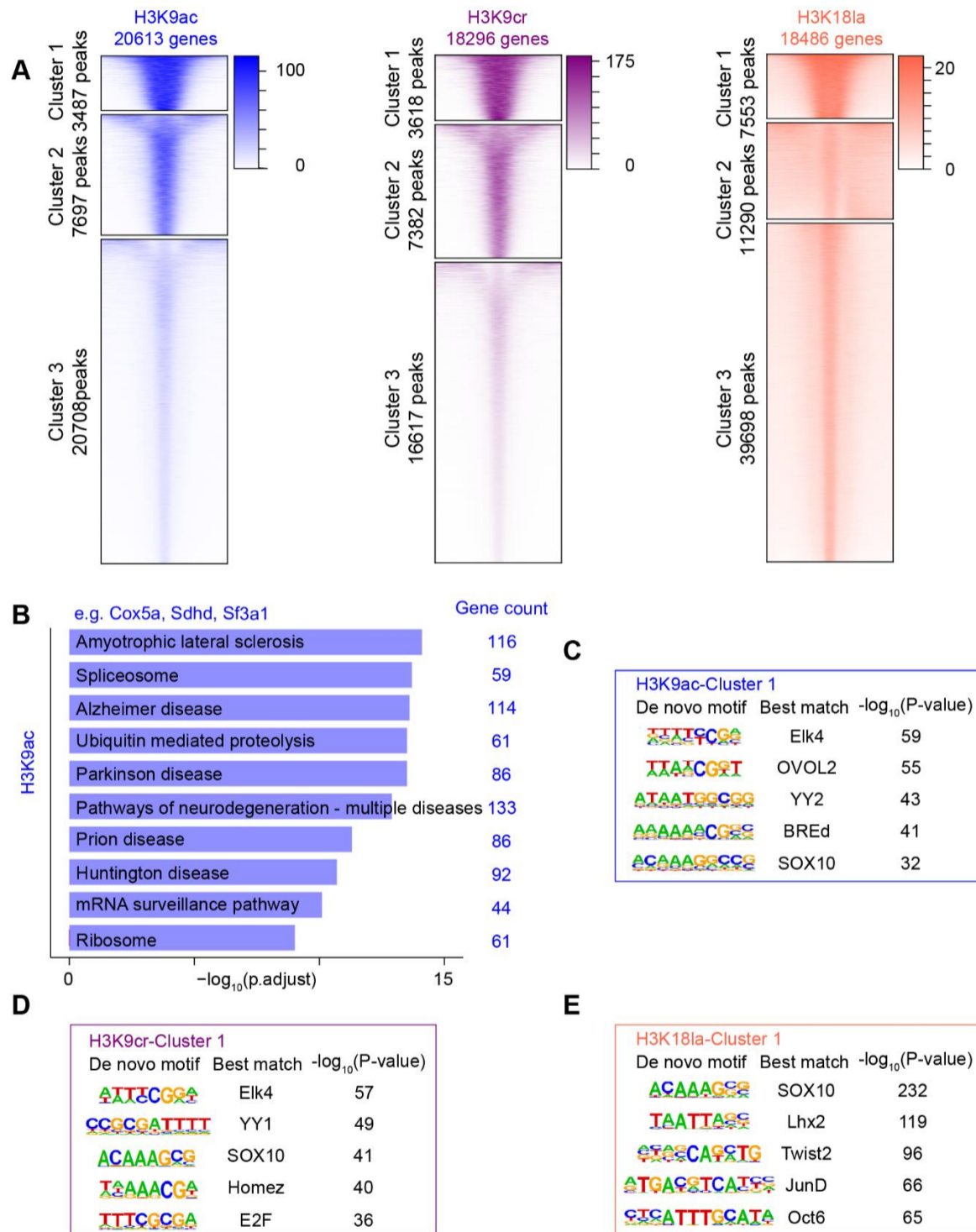
Fig. S4. The cluster and motif analysis of histone acylations peaks. (A) Density heatmaps in the E13.5 telencephalon for H3K9ac (left panel), H3K9cr (middle panel), and H3K18la (right panel) ChIP-seq at ±2.5 kb from the center of peak regions of H3K9ac, H3K9cr, and H3K18la, respectively, which were divided into three clusters and ranked from the highest to the lowest by H3K9ac, H3K9cr, or H3K18la signal, with the number of genes in each cluster labeled on the left. (B) KEGG pathway enrichment analysis of genes under the regulation of H3K9ac (3319 genes) in the E13.5 telencephalon. (C–E) Sequence logos corresponding to enriched elements identified by de novo motif analysis of H3K9ac (C), H3K9cr (D), and H3K18la (E) peaks in the E13.5 telencephalon.
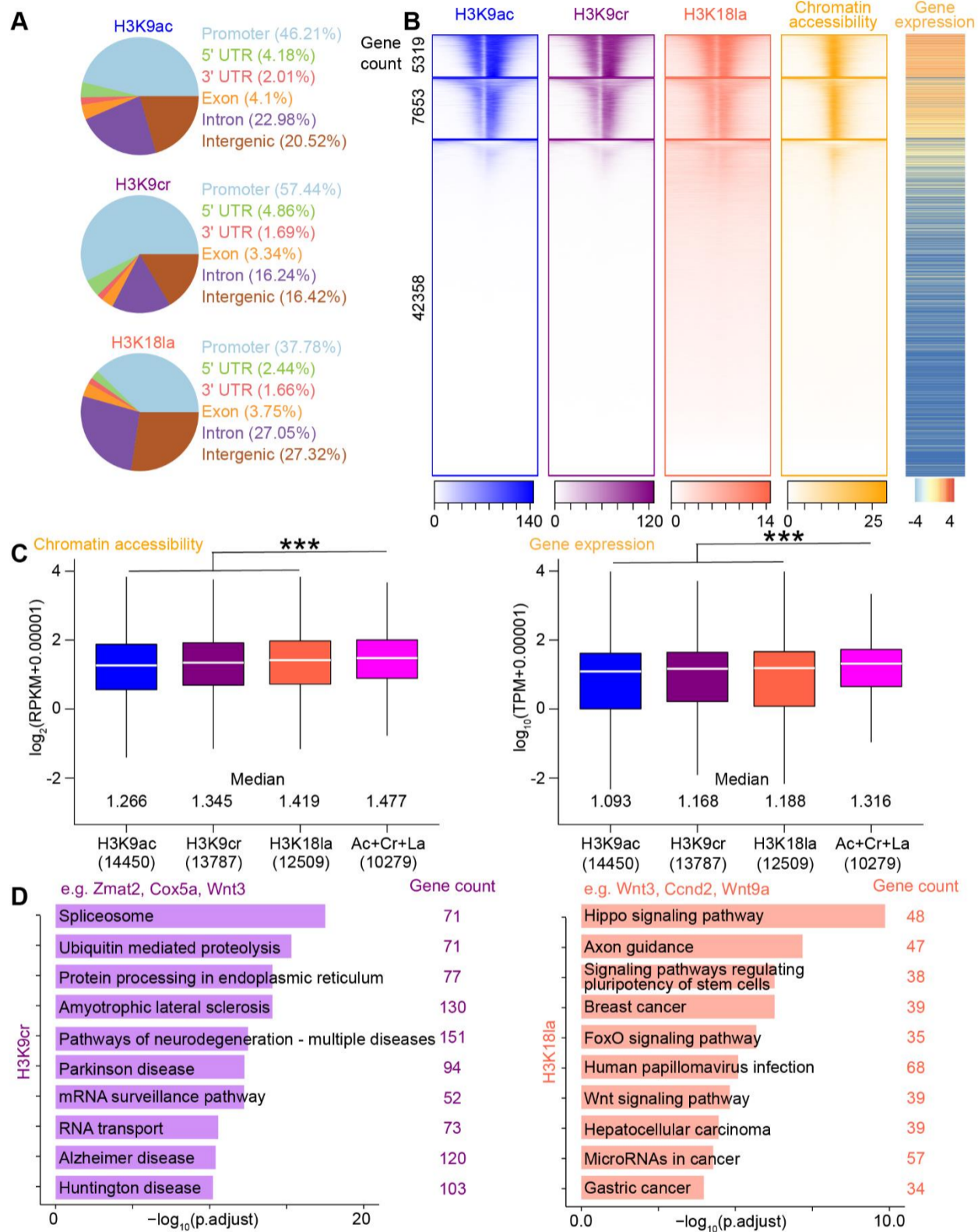
Fig. S5. Multi-omics profiling and functional annotation of H3K9cr and H3K18la in NSPCs. (A) Pie chart showing the distribution of H3K9ac, H3K9cr, and H3K18la peaks in annotated genomic regions in the P19 EC cells-derived day 4 NSPCs. (B) Density heatmaps in the P19 EC cells-derived day 4 NSPCs for H3K9ac, H3K9cr, and

H3K18la ChIP-seq and ATAC-seq at TSSs ± 2.5 kb of annotated genes, which were divided into three clusters and ranked from the highest to the lowest by H3K9ac signal, with the number of genes in each cluster labeled on the left. The heatmap to the right of the density heatmaps displays expression levels (scaled by $\log_{10}$ [TPM+0.00001]) of genes ranked by decreasing H3K9ac signal. (C) Boxplots showing changes in chromatin accessibility levels (left panel) and expression levels (right panel) among different groups of genes in the P19 EC cells-derived day 4 NSPCs. There were 14450, 13787, 12509, and 10279 genes under the regulation of H3K9ac, H3K9cr, H3K18la, and all three histone marks (Ac+Cr+La), respectively. The median for each dataset was noted below each boxplot. Kruskal-Wallis with post hoc Dunn's test was used to analyze statistical significance; ***P <0.001. (D) KEGG pathway enrichment analysis of genes under the regulation of H3K9cr (left panel, 3960 genes) and H3K18la (right panel, 5638 genes) in the P19 EC cells-derived day 4 NSPCs.
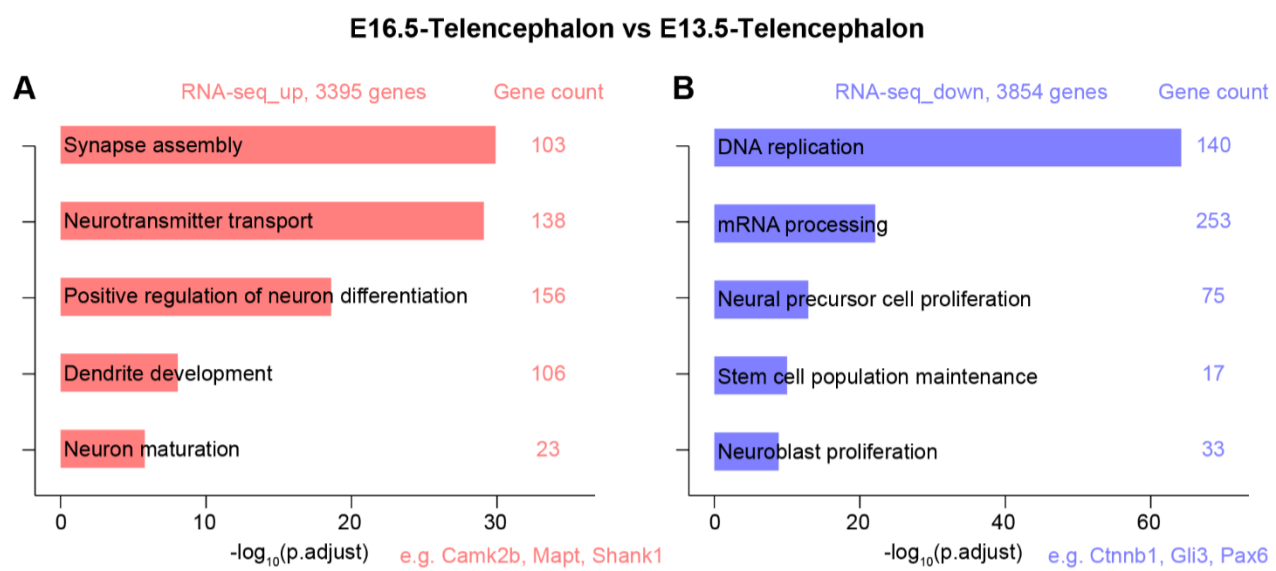
Fig. S6. Enrichment analysis of differentially expressed genes during neural development.

(A, B) GO enrichment analysis (biological process) of upregulated genes (A) and downregulated genes (B) during neural development, which suggested cell fate transitions across different stages of neurogenesis.
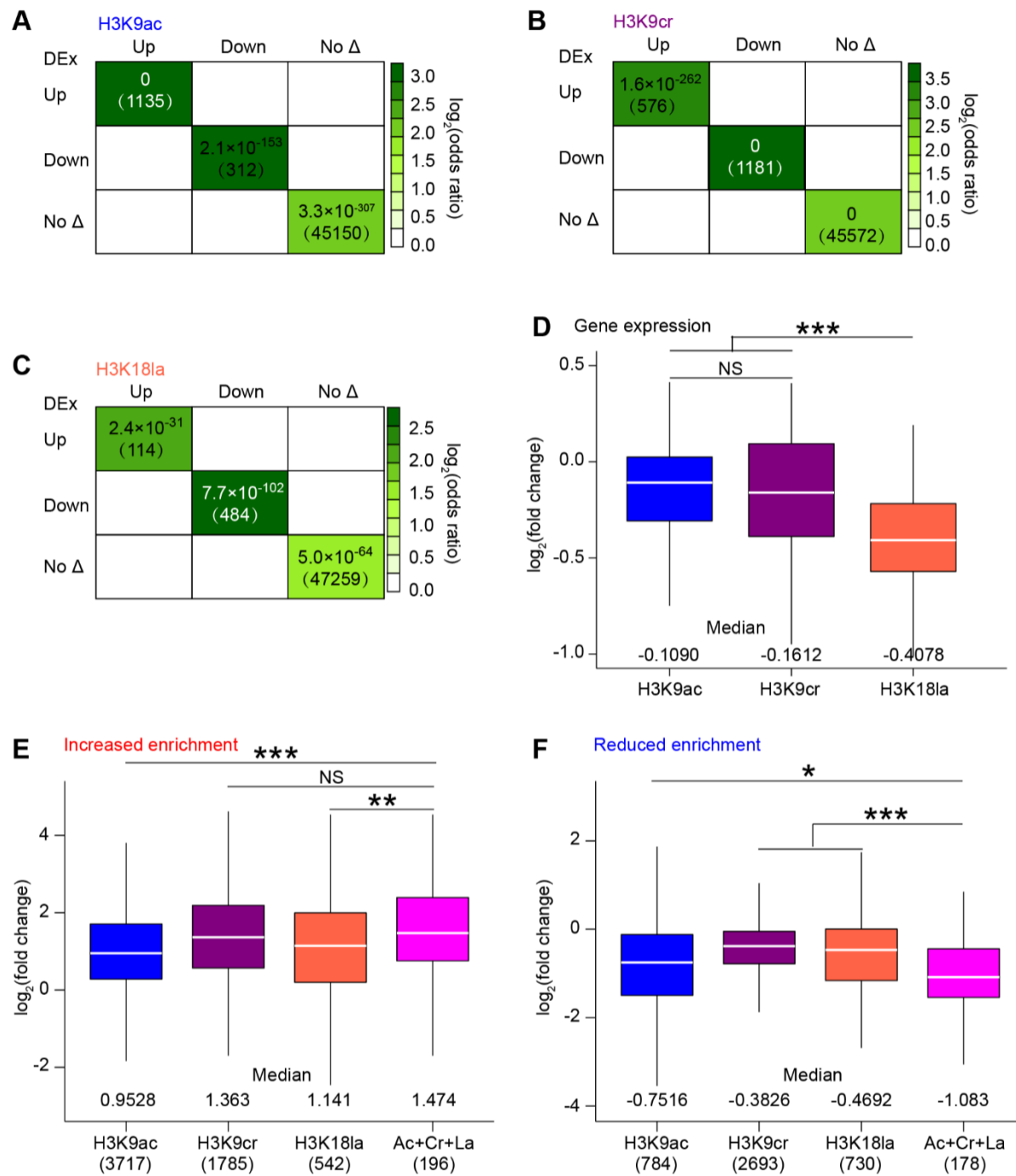
Fig. S7. Dynamic changes in histone acylations at promoter regions. (A–C) Odds-ratio analysis of overlapping genes displaying differential H3K9ac (A), H3K9cr (B), and H3K18la (C) enrichment versus differential expression (DEx), respectively, insert numbers indicate respective P-values for associations, with the number of genes overlapping in parentheses, and two-sided Fisher's exact test was used to analyze statistical significance. (D) Boxplot showing changes in H3K9ac, H3K9cr, and H3K18la enrichment at the promoter regions of 70 genes encoding histones.

The median for each dataset was noted below each boxplot. Kruskal-Wallis with post hoc Dunn's test was used to analyze statistical significance; NS: no significance, ***P <0.001. (E, F) Boxplots showing changes in expression levels among different groups of genes with increased histone acylations (E) and reduced histone acylations (F) at their promoter regions during neural development. There were 3717, 1785, 542, and 196 genes with increased H3K9ac, H3K9cr, H3K18la, and all three histone marks (Ac+Cr+La), respectively. There were 784, 2693, 730, and 178 genes with reduced H3K9ac, H3K9cr, H3K18la, and all three histone marks (Ac+Cr+La), respectively. The median for each dataset was noted below each boxplot. Kruskal-Wallis with post hoc Dunn's test was used to analyze statistical significance; NS: no significance, *P <0.05, **P <0.01, and ***P <0.001.
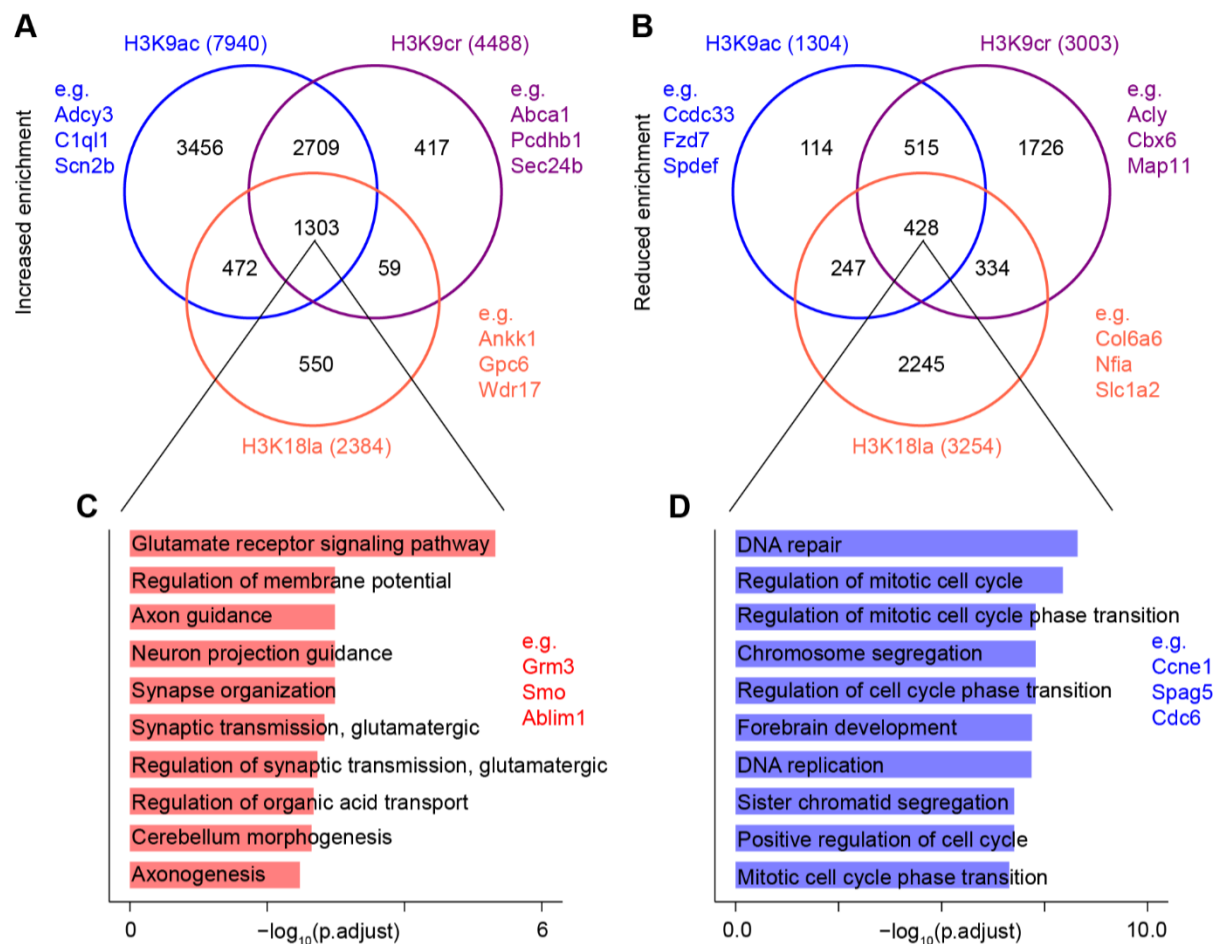
Fig. S8. Dynamic changes in histone acylations at peak regions. (A, B) Venn diagram of a combined comparison of groups of genes with increased H3K9ac, H3K9cr, and H3K18la during neural development (A), and genes with reduced H3K9ac, H3K9cr, and H3K18la during neural development (B). (C, D) GO enrichment analysis (biological process) of 1303 genes with increased H3K9ac, H3K9cr, and H3K18la enrichment (C), and 428 genes with reduced H3K9ac, H3K9cr, and H3K18la enrichment (D), which suggested that multiple histone acylations cooperatively regulated cell fate transitions during neural development.
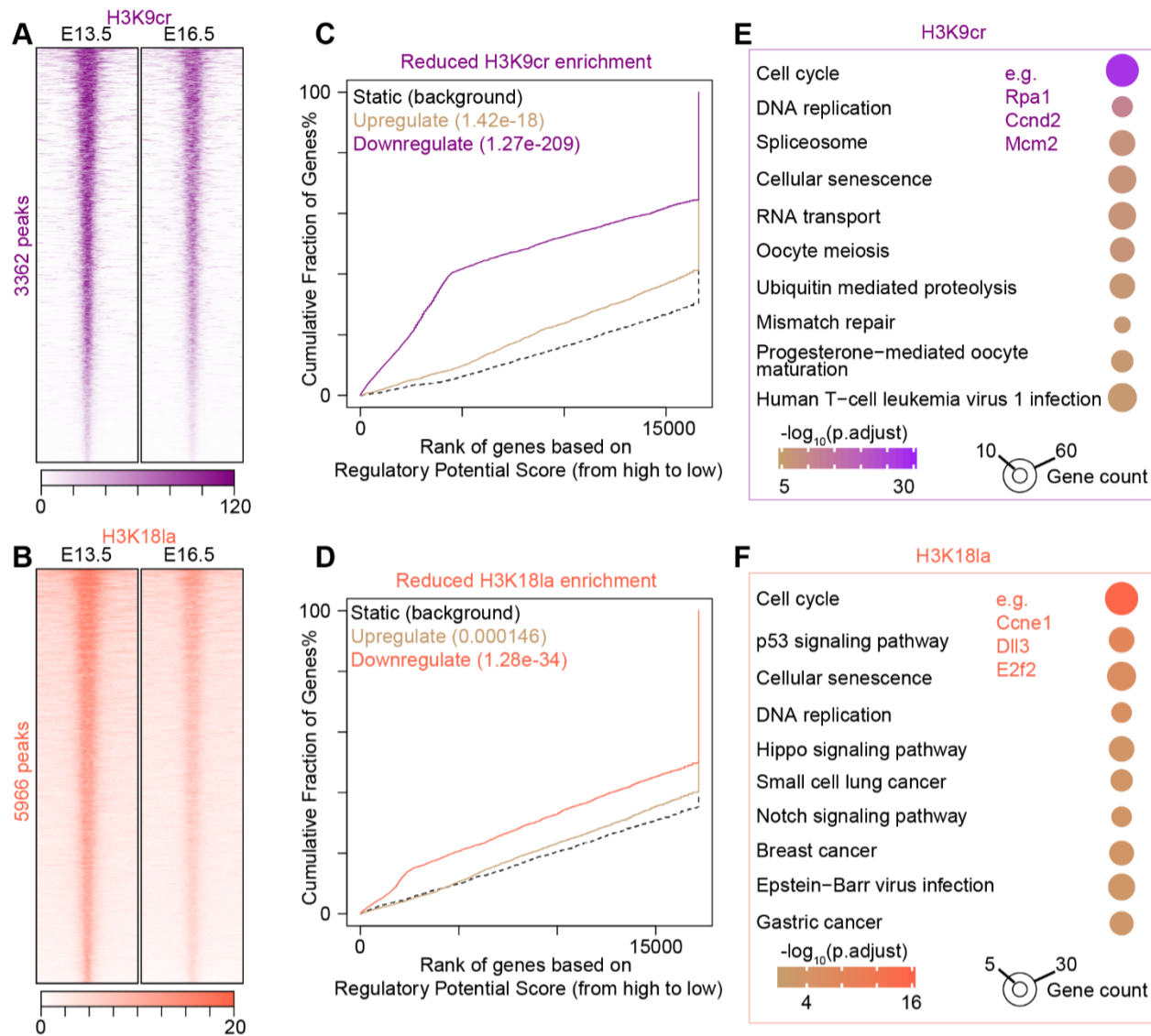
Fig. S9. Associations of histone acylations with cell proliferation during neural development. (A, B) Density heatmaps in the developing telencephalon for H3K9cr (A) and H3K18la (B) ChIP-seq at ± 5 kb from the center of peak regions with reduced H3K9cr (A) and H3K18la (B), respectively, and the number of peaks with differential histone acylations was labeled on the left. (C, D) BETA plot of combined computational analysis of ChIP-seq and RNA-seq data, peak regions with reduced H3K9cr (C) and H3K18la (D) as input. (E, F) KEGG pathway enrichment analysis of downregulated genes with reduced H3K9cr (E) and H3K18la (F) during neural development, there were 1342 and 557 genes in (E) and (F), respectively.
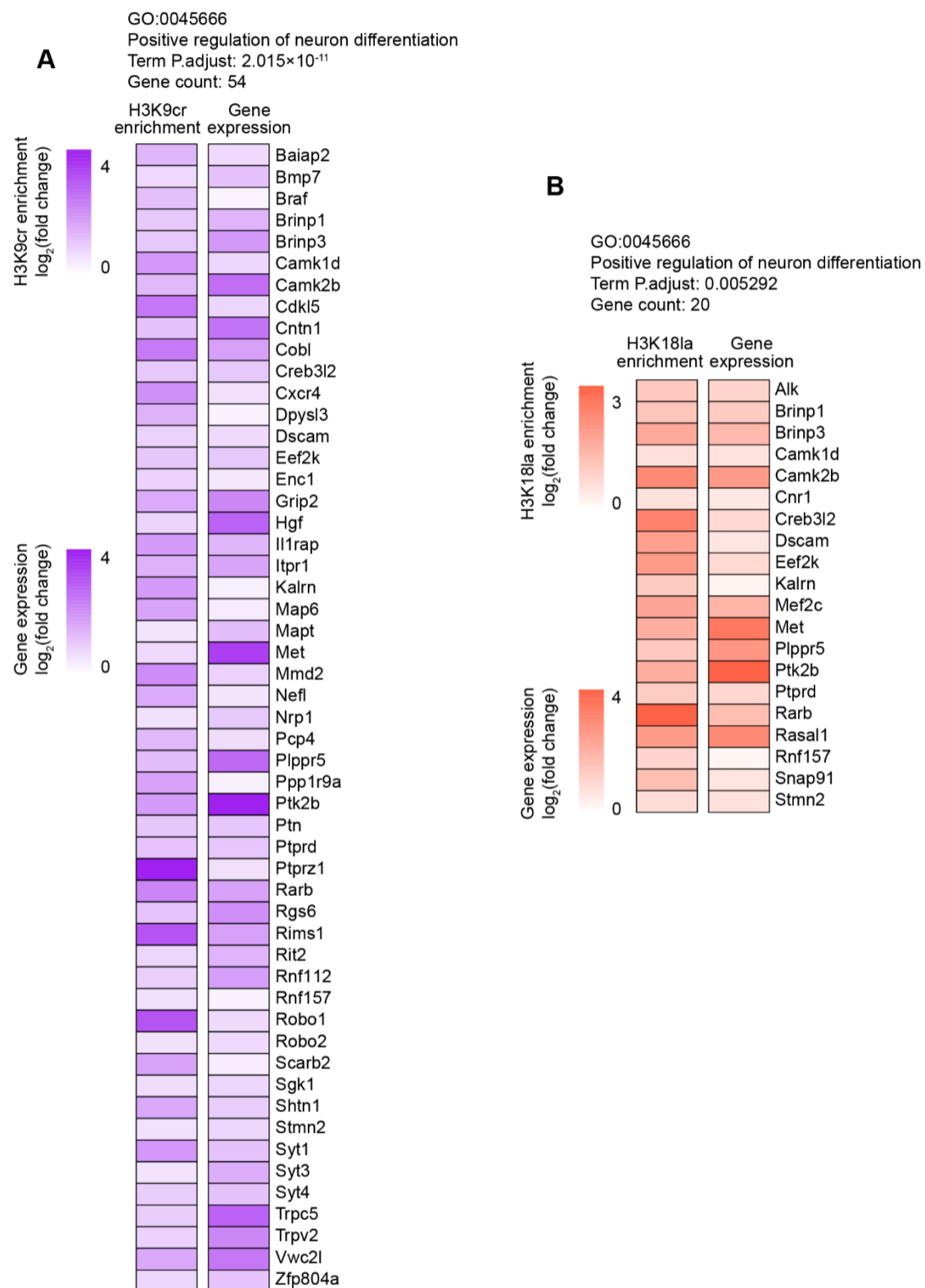
Fig. S10. Associations of histone acylations with neuron differentiation during neural development. (A) Heatmaps shows changes in H3K9cr and expression levels of up-regulated genes with increased H3K9cr enrichment annotated in GO term "positive regulation of neuron differentiation" during neural development. (B) Heatmaps shows changes in H3K18la and expression levels of up-regulated genes with increased H3K18la enrichment annotated in GO term "positive regulation of neuron differentiation" during neural development.
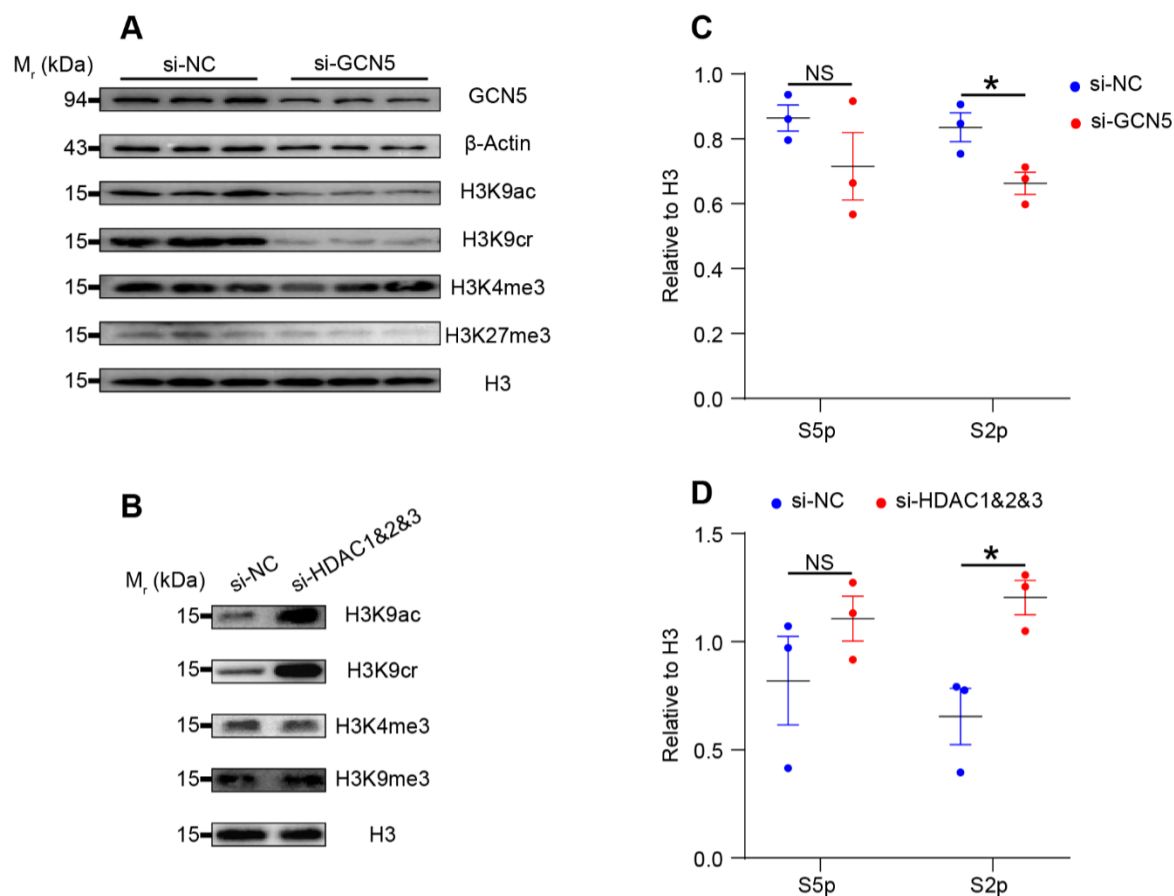
Fig. S11. Changes of histone modifications and transcription after knockdown of *GCN5* and *Hdac1-3*. (A) Blots showing changes in H3K9ac, H3K9cr, H3K4me3, and H3K27me3 levels after knockdown of *GCN5* in 293T cells. (B) Representative blots showing changes in H3K9ac, H3K9cr, H3K4me3, and H3K9me3 levels after knockdown of *Hdac1–3* in P19 EC cells. (C, D) Quantification analysis of changes in nuclear S5p (mark for transcription initiation) and S2p (mark for transcription elongation) levels after knockdown of *GCN5* in 293T cells (C) and *Hdac1-3* in P19 EC cells (D). Data are presented as mean ±SEM of three independent biological replicates, $n = 3$. Unpaired two-tailed Student's t test was used to analyze statistical significance; NS: no significance, $*P < 0.05$.
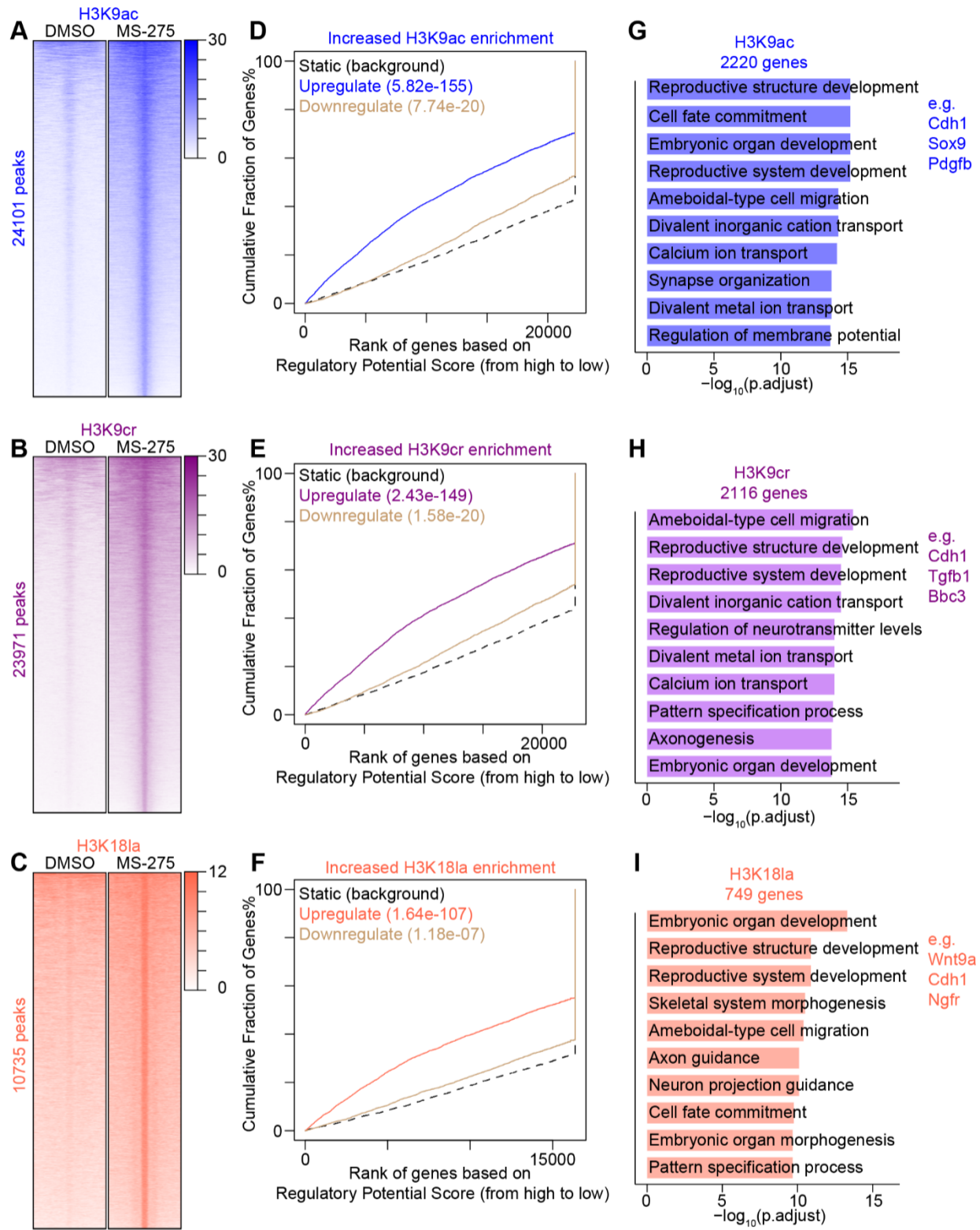
Fig. S12. Genome-wide changes in histone acylations in NSPCs. (A–C) Density heatmaps in the NSPCs for H3K9ac (A), H3K9cr (B), and H3K18la (C) ChIP-seq at ± 5 kb from the center of peak regions with increased H3K9ac (A), H3K9cr (B), and H3K18la (C) after MS-275 treatment in P19 EC cells-derived NSPCs, respectively, and

the number of peaks with differential histone acylations was labeled on the left. (D–F) BETA plot of combined computational analysis of ChIP-seq and RNA-seq data, peak regions with increased H3K9ac (D), H3K9cr (E), and H3K18la (F) after MS-275 treatment in P19 EC cells-derived NSPCs as input. (G–I) GO enrichment analysis (biological process) of upregulated genes with increased H3K9ac (G), H3K9cr (H), and H3K18la (I) after MS-275 treatment in P19 EC cells-derived NSPCs, there were 2220, 2116, and 749 genes in (G), (H), and (I), respectively.
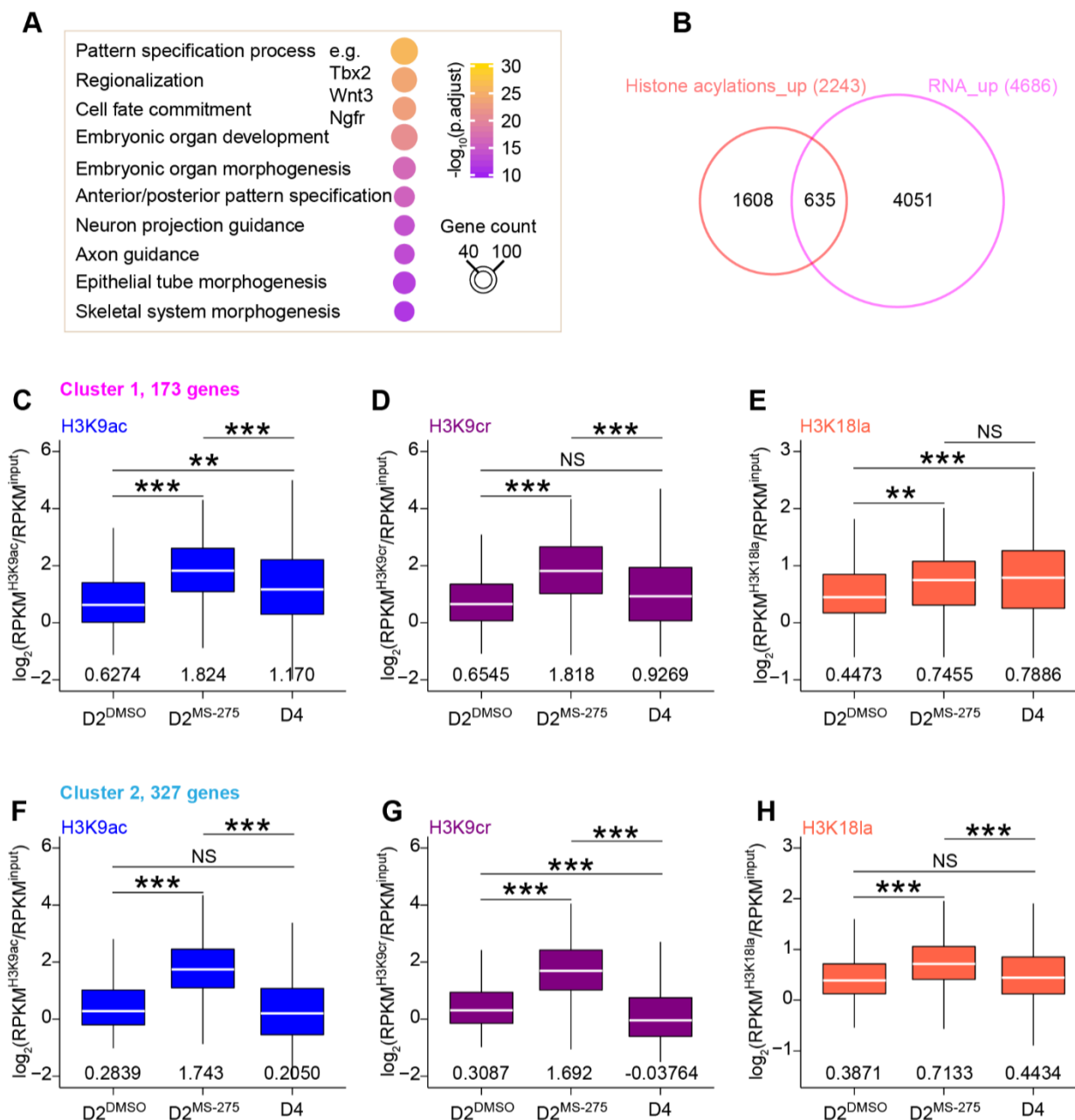
Fig. S13. Histone acylations regulate gene expression in NSPCs. (A) GO enrichment analysis (biological process) of genes with increased H3K9ac, H3K9cr, and H3K18la after MS-275 treatment in P19 EC cells-derived NSPCs. (B) Venn diagram of a combined comparison of groups of genes with increased H3K9ac, H3K9cr, and H3K18la (Histone acylations_up) and genes with upregulated expression (RNA_up) after MS-275 treatment in P19 EC cells-derived NSPCs. (C-E) Boxplot showing changes in H3K9ac (C), H3K9cr (D), and H3K18 (E) enrichment at 171 genes in cluster 1 defined in Fig. 6D, which indicated that genes in cluster 1 got increased histone

acylations in MS-275 treated NSPCs at Day2 (D2^{MS-275}) comparing with that in the DMSO treated control group (D2^{DMSO}), and the increased trends were also observed during normal neural differentiation (D4 [NSPCs at Day4] vs D2^{DMSO}). The median for each dataset was noted below each boxplot. Kruskal-Wallis with post hoc Dunn's test was used to analyze statistical significance; NS: no significance, **P <0.01, ***P <0.001. (F–H) Boxplot showing changes in H3K9ac (F), H3K9cr (G), and H3K18 (H) enrichment at 327 genes in cluster 2 defined in Fig. 6D, which indicated that genes in cluster 2 got increased histone acylations in MS-275 treated NSPCs at Day2 (D2^{MS-275}) comparing with that in the DMSO treated control group (D2^{DMSO}), but the increased trends were not monitored during normal neural differentiation (D4 [NSPCs at Day4] vs D2^{DMSO}). The median for each dataset was noted below each boxplot. Kruskal-Wallis with post hoc Dunn's test was used to analyze statistical significance; NS: no significance, ***P <0.001.
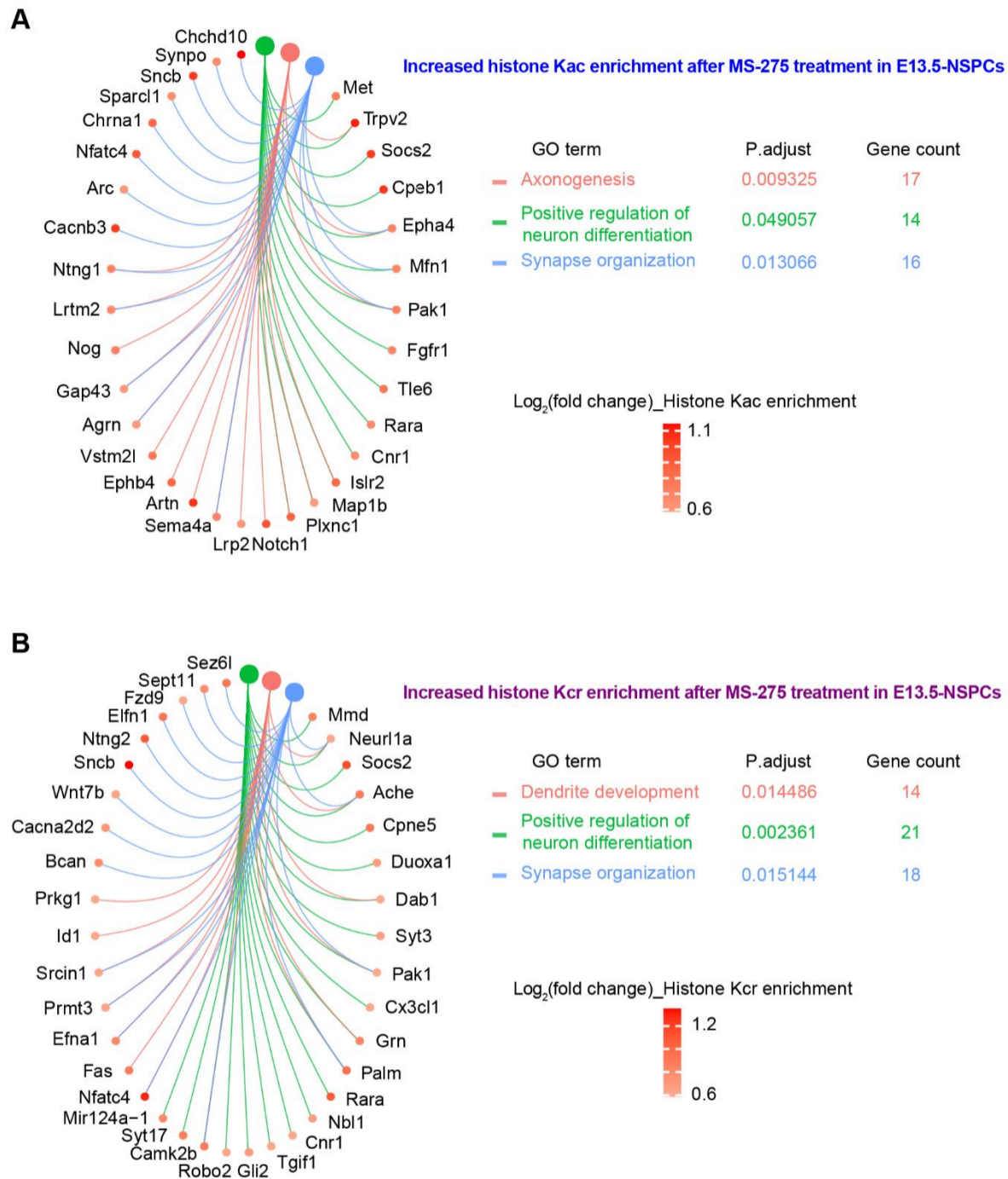
Fig. S14. Dynamic changes in histone Kac and Kcr after MS-275 treatment in embryonic NSPCs. (A, B) Representative terms for GO enrichment analysis (biological process) of genes with increased histone Kac (A) and histone Kcr (B) enrichment after MS-275 treatment in cultured NSPCs isolated from E13.5 mice forebrain, these ChIP-seq datasets were downloaded from GEO databases (GSE124540).
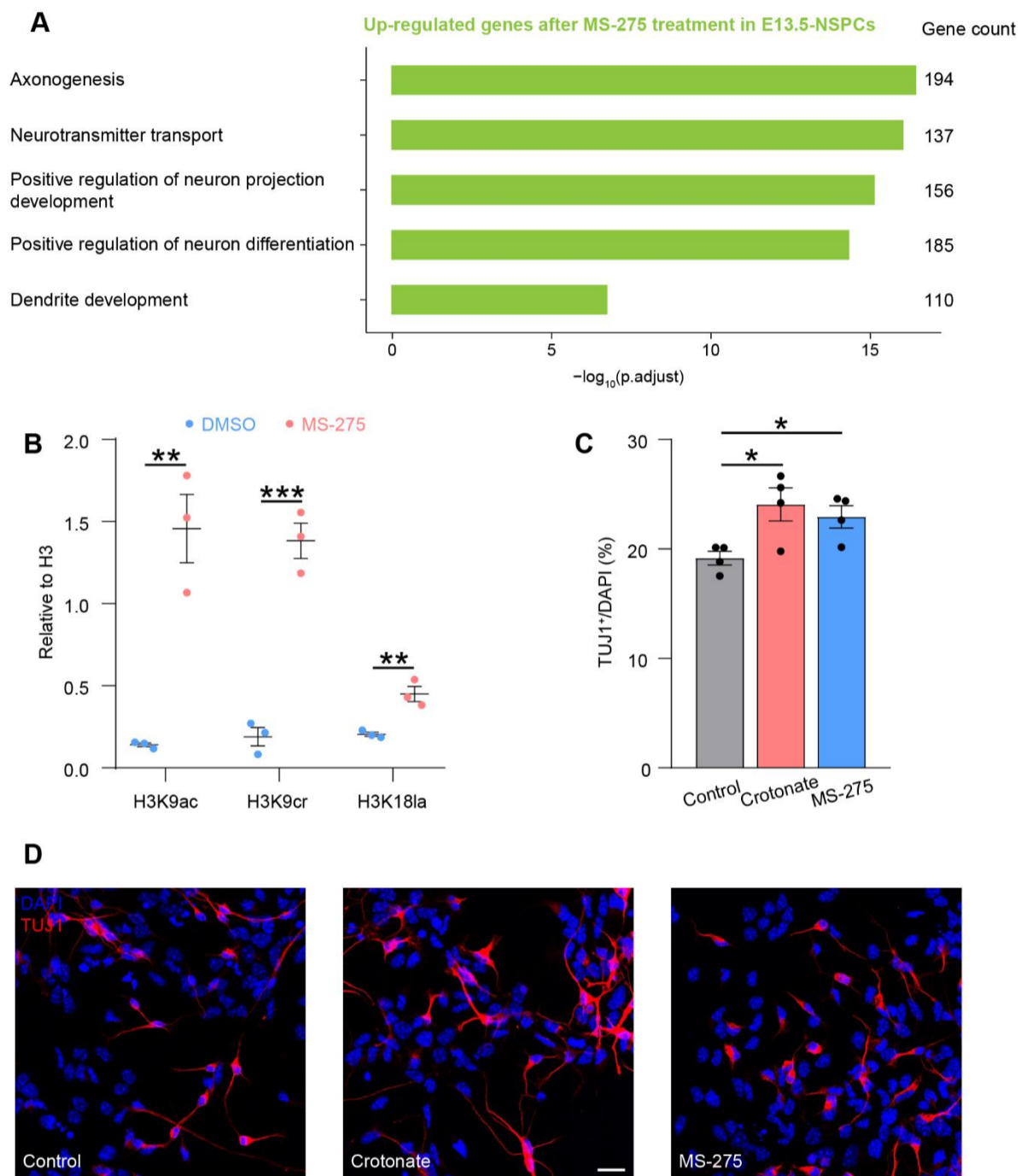
Fig. S15. MS-275 links H3K9cr and H3K18la with neuronal differentiation of NSPCs. (A) Representative terms for GO enrichment analysis (biological process) of genes with up-regulated expression levels after MS-275 treatment in cultured NSPCs isolated from E13.5 mice forebrain, these RNA-seq datasets were downloaded from GEO databases (GSE124540). (B) Quantification analysis of changes in H3K9ac, H3K9cr, and H3K18la levels after MS-275 treatment in NSPCs. Data are presented as mean ± SEM of three independent biological replicates, n = 3. Unpaired two-tailed Studentŝ t test was used to analyze statistical significance; **P <0.01, ****P*P <0.001. (C, D) Quantification analysis (C) and representative images (D) of changes in neuronal differentiation potential defined by TUJ1 positivity among different groups of NSPCs. Scale bar, 20   Data are presented as mean ± SEM of four independent biological replicates, *n* = 4. Two-tailed unpaired Studentŝ t-test was used to analyze statistical significance *P < 0.05.

Table S1. Summary of antibodies used in this study.

Antibody	Purpose	Company	Cat.Number	Dilution
anti-β-Actin	Immunoblot	EASYBIO, Beijing, China	BE0033	1:2000-1:5000
anti-GCN5	Immunoblot	Proteintech	66575-1-Ig	1:1000
anti-H3	Immunoblot	EASYBIO	BE7004	1:2000-1:5000
anti-HDAC1	Immunoblot	Sangon Biotech, Shanghai, China	D260479	1:1000
anti-HDAC2	Immunoblot	Sangon Biotech	D155199	1:1000
anti-HDAC3	Immunoblot	Sangon Biotech	D260481	1:1000
anti-H3K4me3	Immunoblot	Abcam	ab8580	1:1000
anti-H3K9me3	Immunoblot	Millipore	07-442	1:1000
anti-H3K27me3	Immunoblot	Active Motif	39157	1:1000
anti-H3K9ac	ChIP-seq	PTM Biolabs, Hangzhou, China	PTM-156	1.25 µg/ChIP-seq
	Immunoblot			1:1000
anti-H3K9cr	ChIP-seq	PTM Biolabs	PTM-516	1.25 µg/ChIP-seq
	Immunoblot			1:1000
	Immunostaining			1:1000
anti-H3K18cr	Immunoblot	PTM Biolabs	PTM-517	1:2000
	Immunostaining			1:2000
anti-H3K14la	Immunoblot	PTM Biolabs	PTM-1414	1:2000
	Immunostaining			1:2000
anti-H3K18la	ChIP-seq	PTM Biolabs	PTM-1406	3 µg/ChIP-seq
	Immunoblot			1:2000
	Immunostaining			1:2000
Anti-H3K18ac	Immunoblot	PTM Biolabs	PTM-158	1:1000
anti-H3K27ac	Immunoblot	Abcam	ab4729	1:2000
anti-Nestin	Immunostaining	Aves Labs	NES	1:500
anti-Kcr	Immunoblot	PTM Biolabs	PTM-501	1:1000
anti-Kla	Immunoblot	PTM Biolabs	PTM-1401	1:1000
anti-PAX6	Immunoblot	Invitrogen	14-9914	1:1000
anti-PCNA	Immunoblot	Cell Signaling Technology	13110	1:1000
anti RNA pol II CTD repeat phospho S2	Immunoblot	Abcam	ab193468	1:2000
anti RNA pol II CTD repeat phospho S5	Immunoblot	Abcam	ab193467	1:2000
anti-β-Tubulin	Immunoblot	EASYBIO	BE3312	1:2000-1:5000
anti-TUJ1	Immunoblot	BioLegend	801202	1:1000
	Immunostaining			1:1000
donkey anti-rabbit Alexa Fluor 568	Immunostaining	Invitrogen	A10042	1:500
goat anti-chicken Alexa Fluor 594	Immunostaining	Invitrogen	A11042	1:500
goat anti-mouse Alexa Fluor 594	Immunostaining	Invitrogen	A11032	1:500
goat anti-rabbit Alexa Fluor 488	Immunostaining	Invitrogen	A11034	1:500
goat anti-mouse HRP	Immunoblot	EASYBIO	BE0102	1:2000-1:5000
goat anti-rabbit HRP	Immunoblot	EASYBIO	BE0101	1:2000-1:5000

Table S2. List of primer sequence used in this study.

Primer name	Primer sequences (5'–3')
18s rRNA-Forward	GTTGATCCTGCCAGGTAGCA
18s rRNA-Reverse	CAAGTAGGAGAGGAGCGAGC
Actb-Forward	CCATCATGAAGTGTGACGTTGAC
Actb-Reverse	AGGATGCTTAGCTTACCTTGATCTT
Gapdh-Forward	ATGGGTGTGAACCACGAGAAA
Gapdh-Reverse	TCCACTCATGGCAGGGTAAGA

Table S3. Summary of ChIP-seq, ATAC-seq, and RNA-seq data analysis. ChIP-seq

Sample name	Replicate	Total read pairs	Uniquely alignment rate (%)	Overall alignment rate (%)	Total peaks	Regulated genes
E13.5-Telencephalon-H3K9ac	1	53724013	65	99	37319	
E13.5-Telencephalon-H3K9ac	2	51131802	59	98	34532	18574
E13.5-Telencephalon-H3K9cr	1	46817521	61	98	32567	18128
E13.5-Telencephalon-H3K9cr	2	36679840	55	95	28968	18115
E13.5-Telencephalon-H3K18la	1	46396342	78	99	73369	17266
E13.5-Telencephalon-H3K18la	2	39864161	77	99	69157	20519
E16.5-Telencephalon-H3K9ac	1	45849859	67	99	49652	20532
E16.5-Telencephalon-H3K9ac	2	55471433	66	99	50668	20996
E16.5-Telencephalon-H3K9cr	1	44637264	70	97	41074	21138
E16.5-Telencephalon-H3K9cr	2	46975520	73	99	42304	19925
E16.5-Telencephalon-H3K18la	1	45649297	73	99	62073	20141
E16.5-Telencephalon-H3K18la	2	45469142	82	99	76037	18771
E13.5-Telencephalon-input	1	52415013	62	99		20889
E13.5-Telencephalon-input	2	50313387	61	99		
E16.5-Telencephalon-input	1	41469169	61	99		NA
E16.5-Telencephalon-input	2	42552642	61	99		
P19-D4-NSPCs-H3K9ac	1	44385449	78	99	38703	
P19-D4-NSPCs-H3K9ac	2	46237774	78	99	37578	19084
P19-D4-NSPCs-H3K9cr	1	43443207	71	98	29280	18881
P19-D4-NSPCs-H3K9cr	2	43683550	70	98	28707	17196
P19-D4-NSPCs-H3K18la	1	43944019	67	98	54865	17184
P19-D4-NSPCs-H3K18la	2	54241452	71	98	51057	18212
P19-D4-NSPCs-input	1	47291008	66	99		17951
P19-D4-NSPCs-input	2	46914207	65	99		
DMSO_P19-Day 2-H3K9ac	1	46696262	67	98	26555	NA
DMSO_P19-Day 2-H3K9cr	1	47324833	70	97	24874	16495
DMSO_P19-Day 2-H3K18la	1	41266344	66	99	36382	16069
MS-275_P19-Day 2-H3K9ac	1	39077351	72	98	84418	16778
MS-275_P19-Day 2-H3K9cr	1	61457579	63	98	70748	23736
MS-275_P19-Day 2-H3K18la	1	39838816	70	99	31577	22251
DMSO_P19-Day 2-input	1	53034910	56	98		9831
MS-275_P19-Day 2-input	1	47774132	56	98		NA

ATAC-seq

Sample name	Replicate	Total read pairs	Uniquely aligned reads (%)	Overall alignment rate (%)	Total peaks
E13.5-Telencephalon	1	32490761	32	62	26423
E13.5-Telencephalon	2	37379579	30	58	28207
P19-D4-NSPCs	1	42851384	39	96	28399
P19-D4-NSPCs	2	37858578	40	97	24420

RNA-seq

Sample name	Replicate	Total read pairs	Mapping rate (%)
E13.5-Telencephalon	1	20944513	81
E13.5-Telencephalon	2	22718954	81
E16.5-Telencephalon	1	22498548	78
E16.5-Telencephalon	2	23373976	77
P19-D0-ECCs	1	23547414	83
P19-D0-ECCs	2	22022756	83
P19-D4-NSPCs	1	23954541	81
P19-D4-NSPCs	2	22657641	82
P19-D8-Neurons	1	23707915	82
P19-D8-Neurons	2	22849732	81
DMSO_P19-Day 2	1	23809406	82
DMSO_P19-Day 2	2	22205497	82
MS-275_P19-Day 2	1	23019633	82
MS-275_P19-Day 2	2	23174365	81